Reemergence Mechanisms for North Pacific Sea Ice Revealed through Nonlinear Laplacian Spectral Analysis

Mitchell Bushuk, * Dimitrios Giannakis, and Andrew J. Majda

Courant Institute of Mathematical Sciences, New York University, New York, New York

* *Corresponding author address:* Mitch Bushuk, Center for Atmosphere Ocean Science, Courant Institute of Mathematical Sciences, New York University, 251 Mercer Street, New York, NY, 10012.

E-mail: bushuk@cims.nyu.edu

ABSTRACT

This paper studies spatiotemporal modes of variability of sea ice concentration and sea surface temperature (SST) in the North Pacific sector in a comprehensive climate model and observations. These modes are obtained via nonlinear Laplacian spectral analysis (NLSA), a recently developed data analysis technique for high-dimensional nonlinear datasets. The existing NLSA algorithm is modified to allow for a scale-invariant coupled analysis of multiple variables in different physical units. The coupled NLSA modes are utilized to investigate North Pacific sea ice reemergence: a process in which sea ice anomalies originating in the melt season (spring) are positively correlated with anomalies in the growth season (fall) despite a loss of correlation in the intervening summer months. It is found that a low-dimensional family of NLSA modes is able to reproduce the lagged correlations observed in sea ice data from the North Pacific Ocean. This mode family exists in both model output and observations, and is closely related with the North Pacific Gyre Oscillation (NPGO), a low-frequency pattern of North Pacific SST variability. Moreover, this mode family provides a mechanism for sea ice reemergence, in which summer SST anomalies store the memory of spring sea ice anomalies, allowing for sea ice anomalies of the same sign to appear in the fall season. Lagged correlations in model output and observations are significantly strengthened by conditioning on the NPGO mode being active, in either positive or negative phase. Another family of NLSA modes, related to the Pacific Decadal Oscillation (PDO), is found to capture a winter-to-winter reemergence of SST anomalies.

1. Introduction

Sea ice is a complex and critical component of the climate system. Existing at the interface between the atmosphere and the ocean, it modulates the atmosphere's ability to force the ocean through wind, and the ocean's ability to force the atmosphere through sea surface temperatures (SSTs). It also regulates turbulent heat transfer between the two media. Sea ice is a truly multi-scale phenomenon: its dynamics are heavily influenced by large-scale circulation of the ocean and atmosphere, as well as by small-scale thermodynamic and mechanical processes. Understanding the dynamics of sea ice and its relationship to the atmosphere and ocean is of critical importance to twenty-first century scientists, as sea ice is extremely sensitive to greenhouse warming effects (Walsh 1983). Through the ice-albedo feedback mechanism, sea ice has the potential to change rapidly and influence other components of the climate system (Budyko 1969; Curry et al. 1995).

Two regions of high Arctic sea ice variability and interesting sea ice dynamics are the Bering Sea and the Sea of Okhotsk in the North Pacific Ocean. Empirical orthogonal function (EOF) analysis of North Pacific sea ice observational data shows a leading mode which is a sea ice dipole between the Okhotsk and Bering seas, and a second mode with spatially uniform ice changes over the domain (Deser et al. 2000; Liu et al. 2007). Other authors have also found evidence of a Bering-Okhotsk dipole (Cavalieri and Parkinson 1987; Fang and Wallace 1994).

The primary hypothesis from earlier work on North Pacific sea ice is that atmospheric patterns such as the Aleutian low and the Siberian high drive sea ice variability (Parkinson 1990; Cavalieri and Parkinson 1987; Sasaki and Minobe 2006). The study of Blanchard-Wrigglesworth et al. (2011), hereafter BW, suggests that the ocean may also play an important role in sea ice variability. BW found that Arctic sea ice has "memory", in which anomalies of a certain sign in the melt season (spring) tend to produce anomalies of the same sign in the growth season (fall). Additionally, they found that the intervening summer sea ice cover was not strongly correlated with the spring anomalies. This phenomenon, termed sea ice reemergence, was observed in the fall-spring variety described above, as well as a summer-summer reemergence. BW propose a mechanism for the spring-fall reemergence in which spring sea ice anomalies induce an SST anomaly of opposite sign, which persists over the summer months. When the ice edge returns to this spatial location in the fall, the SST anomaly reproduces a sea ice anomaly of the same sign as the spring. The phenomenon of reemergence has also been observed in North Pacific Ocean data (Alexander et al. 1999), in the form of a winter-to-winter SST reemergence.

In this study, we seek an understanding of the coupled variability of sea ice and SST in the North Pacific Ocean. To achieve this, we utilize a recent data analysis technique known as nonlinear Laplacian spectral analysis (NLSA, Giannakis and Majda 2013, 2012c), which is a nonlinear manifold generalization of singular spectrum analysis (SSA, Vautard and Ghil 1989; Broomhead and King 1986; Ghil et al. 2002). Given a time series of high-dimensional data, NLSA yields a set of spatiotemporal modes, analogous to extended EOFs, and a corresponding set of temporal patterns, analogous to principal components (PCs). In applications involving North Pacific SST from climate models (Giannakis and Majda 2012a), these include intermittent type modes not found in SSA that carry low variance but are important as predictor variables in regression models (Giannakis and Majda 2012b).

The original NLSA algorithm was designed for analysis of a single scalar or vector-valued variable, thus modifications to the algorithm are required in order to perform a coupled analysis of multiple variables in different physical units. Here, we investigate the phenomenon of sea ice reemergence using the spatiotemporal modes of variability extracted through coupled NLSA of sea ice concentration and SST from a 900-yr control integration of the Community Climate System Model version 3 (CCSM3, Collins et al. 2006), and in 34 years of sea ice and SST satellite observations from the Met Office Hadley Center Sea Ice and Sea Surface Temperature (HADISST, Rayner et al. 2003) dataset. We find that the sea ice reemergence mechanism suggested by BW can be reproduced in both model output and observations using low-dimensional families of NLSA modes, with the intermittent modes playing a crucial role in this mechanism. Moreover, we find that the reemergence of correlation, in both sea ice and SST, is significantly strengthened by conditioning on certain low-frequency modes being active. These low-frequency modes reflect the North Pacific SST variability of the North Pacific Gyre Oscillation (NPGO, Di Lorenzo et al. 2008) and the Pacific Decadal Oscillation (PDO, Mantua and Hare 2002). We find that the NPGO is related to the sea ice reemergence of BW, while the PDO is related to SST reemergence (Alexander et al. 1999).

The plan of this paper is as follows. In section 2, we introduce the coupled NLSA algorithm. In section 3, we describe the CCSM3 and HADISST datasets. In section 4, we describe modes of variability captured by coupled NLSA when applied to North Pacific sea ice and SST from CCSM3. In section 5, we find reduced subsets of NLSA modes that are able to reproduce the lagged correlation structure of BW, and we provide a mechanism for the observed sea ice memory. We also investigate SST reemergence. In section 6, we compare the results from CCSM3 to observations, by performing similar analyses on the HADISST dataset. We conclude in section 7. Movies illustrating the dynamic evolution of modes are available as online supplementary material.

2. The coupled NLSA algorithm

The original NLSA algorithm (Giannakis and Majda 2013, 2012c) is designed for analysis of a high-dimensional time series from a single scalar or vector-valued variable. This study seeks to perform a coupled analysis of sea ice and SST, thus it was necessary to modify the NLSA algorithm to allow for an analysis of multiple variables with, in general, different physical units.

Let x_t^1 and x_t^2 be two signals, each sampled uniformaly at time step δt. Let x_t^1 be sampled over d_1 gridpoints and x_t^2 be sampled over d_2 gridpoints. Following Giannakis and Majda (2013, 2012c) and the techniques of SSA, we choose some time-lagged embedding window $\Delta t = q\delta t$, and we embed our data in the higher-dimensional space $H_1 = \mathbb{R}^{d_1 q}$ and $H_2 = \mathbb{R}^{d_2 q}$

under the delay-coordinate mappings

$$x_t^1 \mapsto X_t^1 = (x_t^1, x_{t-\delta t}^1, ..., x_{t-(q-1)\delta t}^1),$$
$$x_t^2 \mapsto X_t^2 = (x_t^2, x_{t-\delta t}^2, ..., x_{t-(q-1)\delta t}^2).$$

Next, for each variable we compute the phase space velocities, ξ_i^1 and ξ_i^2, viz.

$$\begin{aligned} \xi_i^1 &= X_i^1 - X_{i-1}^1, \\ \xi_i^2 &= X_i^2 - X_{i-1}^2. \end{aligned} \tag{1}$$

These vectors have a natural geometric interpretation as the vector field on the data manifold driving the dynamics (Giannakis 2014).

NLSA algorithms utilize a set of natural orthonormal basis functions on the nonlinear data manifold to describe temporal patterns analogous to PCs. These basis functions are eigenfunctions of a graph Laplacian operator (see (3), ahead) computed from a pairwise kernel function K on the data. The graph Laplacian eigenfunctions form a complete basis on the data manifold and are ordered in terms of increasing eigenvalue. These eigenvalues can be interpreted as squared "wavenumbers" on the data manifold (Giannakis and Majda 2014). Performing a spectral truncation in terms of the leading l eigenfunctions acts as a filter for the data, which removes high wavenumber energy, while retaining the energy at low wavenumbers. This truncation penalizes highly oscillatory features on the data manifold, and emphasizes slowly varying ones.

In the coupled NLSA approach introduced here, the pairwise kernel function K is constructed using the idea of scale invariance. In particular, we compute the Gaussian kernel K_{ij} so that physical variables are made dimensionless, allowing for direct comparison of different variables:

$$K_{ij} = \exp\left(-\frac{\|X_i^1 - X_j^1\|^2}{\epsilon\|\xi_i^1\|\|\xi_j^1\|} - \frac{\|X_i^2 - X_j^2\|^2}{\epsilon\|\xi_i^2\|\|\xi_j^2\|} \right). \tag{2}$$

Here, ϵ is a parameter that controls the locality of the Gaussian kernel, and $\|\cdot\|$ is the standard Euclidean norm. Heuristically, K_{ij} represents the likelihood of a random walker on the data manifold transitioning from state i to state j. Note that this random walk is introduced solely for the purpose of evaluating orthonormal basis functions on the discrete data manifold. In particular, the random walk has no relation to the actual dynamics of the system. This kernel depends on the phase velocity magnitude $\|\xi_i\|$ from (1) in the sense that states with a large (small) velocity magnitude have appreciable transition probability to a larger (smaller) number of states, due to the Gaussian having a larger (smaller) width. As a result, the algorithm has enhanced skill in capturing transitory events characterized by large $\|\xi_i\|$ (Giannakis and Majda 2012c). Using the graph Laplacian approach of Coifman and Lafon (2006), we compute the Laplacian matrix L via the following steps:

$$
\begin{aligned}
Q_i &= \sum_{j=1}^{s-q} K_{ij}, \\
\tilde{K}_{ij} &= \frac{K_{ij}}{Q_i^\alpha Q_j^\alpha}, \\
D_i &= \sum_{j=1}^{s-q} \tilde{K}_{ij}, \\
P_{ij} &= \frac{\tilde{K}_{ij}}{D_i}, \\
L &= I - P,
\end{aligned}
$$

where P is a transition matrix, I is the identity matrix, and α is a normalization parameter. For this study, we will use $\alpha = 0$, which is a conventional choice for this class of algorithms.

From here, the algorithm proceeds analogously to NLSA. We solve the eigenvalue problem

$$
L\phi_i = \lambda\phi_i, \tag{3}
$$

and recover a set of discrete Laplacian eigenfunctions $\{\phi_1, \phi_2, \ldots, \phi_{s-q}\}$ defined on the data manifold. The transition matrix P also defines an invariant measure $\vec{\mu}$ on the discrete data manifold, given by

$$
\vec{\mu} P = \vec{\mu},
$$

where μ_i represents the volume occupied by the sample $X_i = (X_i^1,\, X_i^2)^t$ on the data manifold.

Let $X^1 : \mathbb{R}^{s-q} \mapsto \mathbb{R}^{qd_1}$ and $X^2 : \mathbb{R}^{s-q} \mapsto \mathbb{R}^{qd_2}$ be the data matrices for our two s-sample data sets:

$$X^1 = \begin{bmatrix} X^1_{q+1} & X^1_{q+2} & \dots & X^1_s \end{bmatrix},$$
$$X^2 = \begin{bmatrix} X^2_{q+1} & X^2_{q+2} & \dots & X^2_s \end{bmatrix}.$$

Projecting X^1 and X^2 onto the leading l Laplacian eigenfunctions, we construct linear maps $A^1_l : \mathbb{R}^l \mapsto \mathbb{R}^{qd_1}$ and $A^2_l : \mathbb{R}^l \mapsto \mathbb{R}^{qd_2}$, given by

$$A^1_l = X^1 \mu \Phi, \quad A^2_l = X^2 \mu \Phi.$$

In the above, Φ is a matrix whose columns are the leading l Laplacian eigenfunctions, and μ is a diagonal matrix with entries $\vec{\mu}$ along the diagonal. Singular value decomposition (SVD) of the operators A^1_l and A^2_l yields sets of spatiotemporal modes u^1_k and u^2_k of dimension qd_1 and qd_2, respectively, analogous to extended EOFs, and temporal modes $v^1_k(t)$ and $v^2_k(t)$ of length $s - q$, analogous to PCs. Projecting the modes from lagged embedding space to physical space, we obtain spatiotemporal patterns $\tilde{u}^1_k(t)$ and $\tilde{u}^2_k(t)$ for the two original fields.

It should be noted that, while the SVD is performed on each operator individually, the resulting spatiotemporal patterns $\{u^1_k\}$ and $\{u^2_k\}$, and principal components $\{v^1_k\}$ and $\{v^2_k\}$, are inherently coupled. This is because these operators are constructed using the same l-dimensional set of eigenfunctions, which have been computed using the full multivariate dataset.

Another natural possibility for performing coupled NLSA is to perform an initial normalization of each physical variable to unit variance, and subsequently perform the standard NLSA algorithm on the concatenated dataset. A problem with this approach is that we artificially impose the variance ratio of the two variables, without incorporating any information about their relative variabilities. An appealing feature of the coupled approach described above is that the variance ratio between variables is automatically chosen by the algorithm in a dynamically motivated manner. We term the approach outlined in this section "phase velocity normalization" and the normalization to unit variance "variance normalization." We will return to these issues in section 4a. Another appealing aspect of the algorithm above is that it can be naturally generalized from two variables to many variables.

3. Dataset description

a. CCSM3 model output

This study analyzes model output from a 900-yr equilibrated control integration of CCSM3 (Collins et al. 2006). We use CCSM3 monthly averaged sea ice concentration and SST data, which come from the Community Sea Ice Model (CSIM, Holland et al. 2006) and the Parallel Ocean Program (POP, Smith and Gent 2004), respectively. The model uses a T42 spectral truncation for the atmospheric grid (roughly $2.9° \times 2.9°$), and the ocean and sea ice variables are defined on the same grid, of 1° nominal resolution. This study focuses on the North Pacific sector of the ocean, which we define as the region 120°E–110°W and 20°N–65°N (Teng and Branstator 2011). Note that the seasonal cycle has not been removed from this dataset.

Sea ice concentration is only defined for the northern part of this domain, thus we have $d_1 = 3750$ sea ice spatial gridpoints, and $d_2 = 6671$ SST spatial gridpoints. Using an embedding window of $q = 24$ (Giannakis and Majda 2012c), this yields lagged embedding dimensions of $qd_1 = 90{,}000$ and $qd_2 = 160{,}104$. The value of $q = 24$ months was used as the time lag because the resulting embedding window is longer than the seasonal cycle, which is a primary source of non-Markovianity in this dataset. A number of q values $\in [1, 48]$ were tested, including q's relatively prime to 12. It was found that the results were qualitatively similar for sufficiently large q, i.e. $q \geq 12$, and sensitive to q for $q < 12$ (see also Giannakis and Majda 2013).

b. Observational data

We also study the Met Office Hadley Center Sea Ice and Sea Surface Temperature (HadISST) dataset (Rayner et al. 2003), which consists of monthly averaged sea ice and SST data on a 1° latitude-longitude grid. We use the satellite era data from January 1979-August 2013. Note that all ice-covered gridpoints in the HADISST dataset were assigned an SST value of -1.8°C, the freezing point of salt water at a salinity of 35 parts per thousand. Moreover, the trend in the dataset was removed by computing a long-term linear trend for each month of the year, and removing the respective linear trend from each month.

4. Coupled sea ice-SST spatiotemporal modes of variability in CCSM3

We apply the coupled NLSA algorithm described in Section 2 to the CCSM3 sea ice and SST datasets, using an embedding window of $\Delta t = 24$ months, and choosing the parameter ϵ, which controls the locality of the Gaussian kernel, as $\epsilon = 1.4$. We include a discussion of the of the robustness of results with respect to changes in ϵ in section 4a. Note that the time mean at each gridpoint has been subtracted from the dataset, but the seasonal cycle has not been subtracted. Utilizing the spectral entropy criterion outlined in Giannakis and Majda (2012a, 2013), we choose a truncation level of $l = 22$, and express the lagged embedding matrices X^{ICE} and X^{SST} in the basis of the leading 22 Laplacian eigenfunctions, yielding the operators A_l^{ICE} and A_l^{SST}. Singular value decomposition of A_l^{ICE} produces a set of l temporal patterns, v_k^{ICE}, of length $s - q$, analogous to PCs and l corresponding spatiotemporal patterns, u_k^{ICE}, of dimension qd_1, analogous to extended EOFs. Similarly, SVD of A_l^{SST} produces temporal patterns, v_k^{SST}, and corresponding spatiotemporal patterns u_k^{SST}, of dimension qd_2. Each variable has its own set of principal components, but we find that each sea ice PC is strongly correlated with a particular SST PC. Therefore, it is natural to consider the corresponding spatiotemporal patterns as a pattern of coupled SST-sea ice variability.

Figure 1a shows the singular values of the operators A_l^{ICE} and A_l^{SST} using the phase velocity normalization approach outlined in section 2 and the variance normalization approach mentioned at the end of section 2. Also shown are the singular values from SSA performed on the unit variance normalized dataset. Note that the SST singular values decay much more rapidly than the sea ice singular values, indicating that the SST signal has more variability stored in its leading modes than the sea ice signal.

Figure 1b shows a plot of the normalized relative entropy vs truncation level l, computed using the approach of Giannakis and Majda (2012a, 2013). As $l \to \infty$, and in the case of uniform measure $\vec{\mu}$ and phase velocity ξ, the results of NLSA converge to SSA. The spectral entropy criterion provides a heuristic guideline for choosing l, designed to select l large-enough to reproduce the crucial features of the data, but small-enough to filter out highly oscillatory features of the data (Giannakis and Majda 2014). The latter would be present in the SSA limit mentioned above. In the normalized relative entropy plot, spikes represent the addition of qualitatively new features to the data, and suggest possible truncation levels. Here, seeking a parsimonious description of the data, we select a truncation level of $l = 22$.

a. *Temporal modes and sea ice-SST coupling*

Coupled NLSA yields three distinct families of of modes: periodic, low-frequency, and intermittent modes. Figures 2 and 3 summarize the temporal patterns v_k^{ICE} and v_k^{SST}, respectively, showing snapshots of the v_k^{ICE} and v_k^{SST} time series, power spectral densities, and autocorrelation functions. We use the letters P, L, and I to designate periodic, low-frequency, and intermittent modes, respectively.

The periodic modes exist in doubly degenerate pairs with temporal patterns $v_k(t)$ that are sinusoidal with a relative phase of $\pi/2$, and with frequencies of integer multiples of 1 yr^{-1}. The leading two pairs of periodic modes carry more variance than any of the low-frequency or intermittent modes, and represent annual and semiannual variability, respectively. The low-frequency modes carry the majority of their spectral power over interannual to decadal timescales, and have a typical decorrelation time of 3–4 years.

The intermittent modes are characterized by broadband spectral power centered on a base frequency of oscillation with some bias towards lower frequencies. Similar to the periodic modes, these modes come in nearly degenerate pairs. The temporal behavior of the intermittent modes resembles a periodic signal modulated by a low frequency envelope. In the spatial domain, they are characterized by a bursting-type behavior with periods of quiescence followed by periods of strong activity. The intermittent modes carry lower variance than their low-frequency and periodic counterparts (see Fig. 1a), however they play a crucial role in explaining the sea ice reemergence mechanism, as will be demonstrated in the following sections of this paper. Elsewhere (Giannakis and Majda 2012b), it has been demonstrated that this class of modes has high significance in external-factor regression models for low-frequency modes, in which the intermittent modes are used as prescribed external factors (forcings). Intermittent type modes highlight the main difference between SSA and NLSA: NLSA captures low-variance patterns of potentially high dynamical significance using a small set of modes, while classical SSA does not.

The sea ice PCs, v_k^{ICE}, are certainly not independent of the SST PCs, v_k^{SST}. We find that each sea ice PC is strongly correlated with a certain SST PC. In Fig. 4, we show correlations between selected sea ice and SST PCs. Motivated by these correlations, we define the following coupled modes of sea ice-SST variability: $\mathbf{P}_1 = (P_1^{\mathrm{ICE}}, P_1^{\mathrm{SST}})$, $\mathbf{P}_2 = (P_2^{\mathrm{ICE}}, P_2^{\mathrm{SST}})$, $\mathbf{P}_3 = (P_3^{\mathrm{ICE}}, P_3^{\mathrm{SST}})$, $\mathbf{P}_4 = (P_4^{\mathrm{ICE}}, P_4^{\mathrm{SST}})$, $\mathbf{L}_1 = (L_1^{\mathrm{ICE}}, L_2^{\mathrm{SST}})$, $\mathbf{L}_2 = (L_3^{\mathrm{ICE}}, L_1^{\mathrm{SST}})$, $\mathbf{I}_1 = (I_1^{\mathrm{ICE}}, I_3^{\mathrm{SST}})$, $\mathbf{I}_2 = (I_2^{\mathrm{ICE}}, I_4^{\mathrm{SST}})$, $\mathbf{I}_3 = (I_3^{\mathrm{ICE}}, I_2^{\mathrm{SST}})$, $\mathbf{I}_4 = (I_4^{\mathrm{ICE}}, I_1^{\mathrm{SST}})$, $\mathbf{I}_5 = (I_5^{\mathrm{ICE}}, I_8^{\mathrm{SST}})$, $\mathbf{I}_6 = (I_6^{\mathrm{ICE}}, I_7^{\mathrm{SST}})$, $\mathbf{I}_7 = (I_7^{\mathrm{ICE}}, I_6^{\mathrm{SST}})$, and $\mathbf{I}_8 = (I_8^{\mathrm{ICE}}, I_5^{\mathrm{SST}})$. Note that the mode pairs $\{\mathbf{P}_1, \mathbf{P}_2\}$, $\{\mathbf{P}_3, \mathbf{P}_4\}$, $\{\mathbf{I}_1, \mathbf{I}_2\}$, $\{\mathbf{I}_3, \mathbf{I}_4\}$, $\{\mathbf{I}_5, \mathbf{I}_6\}$, and $\{\mathbf{I}_7, \mathbf{I}_8\}$ are degenerate modes with a relative phase of $\pi/2$.

A number of different values of ϵ, the locality parameter of the Gaussian kernel, were tested to examine the robustness of these results. We find that the modes are very similar for values of $\epsilon \in [1, 2]$. For values of ϵ outside this interval, we observe a less clean split between $\mathbf{L}_2$ and certain intermittent modes, resulting in modes with power spectra that resemble a combination of the low-frequency and intermittent modes. We find that the periodic modes and modes $\{\mathbf{L}_1, \mathbf{I}_1, \mathbf{I}_2, \mathbf{I}_5, \mathbf{I}_6\}$, which will be important later in the paper, are much more robust with respect to changes in ϵ. These modes are very similar for values of $\epsilon \in [0.5, 5]$.

b. Spatiotemporal modes

Figure 5 shows the spatial patterns of the coupled modes defined above at a snapshot in time. Movie 1, showing the evolution of these spatial patterns, is available in the online supplementary material, and is much more illuminating.

1) Periodic modes

The pair of annual periodic modes, $\{\mathbf{P}_1, \mathbf{P}_2\}$, have a sea ice pattern which involves spatially uniform growth in the Bering and Okhotsk Sea from October to March and spatially uniform melt from April to September. The SST pattern is intensified in the western part of the basin and along the West Coast of North America. Moreover, it is relatively uniform zonally, and out of phase with the annual periodic sea ice anomalies. The semiannual pair of modes, $\{\mathbf{P}_3, \mathbf{P}_4\}$, have a sea ice pattern with strong amplitude in the southern part of the Bering and Okhotsk seas and much weaker amplitude in the northern part of these seas. The SST pattern of these modes is, again, relatively uniform zonally and intensified in the western part of the basin. The higher-frequency periodic modes have more spatial structure and zonal variability, as well as smaller amplitude.

2) Low-frequency modes

The leading low-frequency mode, $\mathbf{L}_1$, has an SST pattern that resembles the NPGO (Di Lorenzo et al. 2008), which is the second leading EOF of seasonally detrended Northeast

Pacific (180°W – 110°W and 25°N – 62°N) SST. Computing pattern correlations between EOFs of Northeast Pacific SST and the q SST spatial patterns of $\mathbf{L}_1$, we find a maximum pattern correlation of 0.94 with EOF 2, the NPGO mode. If we consider basin-wide SST patterns, we find that the SST pattern of $\mathbf{L}_1$ has a maximum pattern correlation of 0.82 with EOF 3 of North Pacific (120°E – 110°W and 20°N – 65°N) SST. EOF 3 has a pattern correlation of 0.91 with the NPGO, thus this mode seems to reflect the basin-wide pattern of variability corresponding to the NPGO mode of the Northeast Pacific. In light of these correlations, we call $\mathbf{L}_1$ the NPGO mode. Note that these SST EOFs were computed using SST output from the CCSM3 model. The NPGO mode has its dominant sea ice signal in the Bering Sea, and its amplitude is largest in the southern part of the Bering Sea. Its SST pattern has a strong anomaly of opposite sign, spatially coincident with the sea ice anomaly, as well as a weaker anomaly extending further southward and eastward in the domain.

The second low-frequency mode, $\mathbf{L}_2$, has a spatial pattern resembling the PDO, which is the leading EOF of seasonally detrended North Pacific SST data (Mantua and Hare 2002). Computing pattern correlations between EOF 1 of North Pacific SST (the PDO) and the SST pattern of $\mathbf{L}_2$, we find a maximum pattern correlation of 0.99. Also, EOF 1 of Northeast Pacific SST (which has a 0.99 pattern correlation with the PDO) has a maximum pattern correlation of 0.98 with the SST pattern of $\mathbf{L}_2$. In light of these correlations, we call $\mathbf{L}_2$ the PDO mode. The sea ice component of the PDO mode consists of sea ice anomalies along the Kamchatka Peninsula, and in the southern and eastern parts of the Sea of Okhotsk. The SST pattern consists of a large-scale SST anomaly along the Kuroshio extension region, and an anomaly of the opposite sign along the west coast of North America.

3) Intermittent modes

The leading pair of intermittent modes, $\{\mathbf{I}_1, \mathbf{I}_2\}$, have a base frequency of 1 yr^{-1} and are characterized by a strong pulsing sea ice anomaly in the southern Bering Sea and a weaker anomaly of opposite sign in the Sea of Okhotsk. The SST pattern consists of a strong pulsing dipole anomaly in the Bering Sea and weaker small-scale temperature anomalies that propagate eastward along the Kuroshio extension region. The next pair of annual intermittent modes, $\{\mathbf{I}_3, \mathbf{I}_4\}$, have sea ice anomalies that originate in the Bering Sea and propagate along the Kamchatka peninsula into the Sea of Okhotsk. The SST pattern is a basin-wide signal, with strong intermittent anomalies along the Kuroshio extension region, as well as in the Sea of Okhotsk and Bering Sea. The semiannual intermittent mode pairs $\{\mathbf{I}_5, \mathbf{I}_6\}$ and $\{\mathbf{I}_7, \mathbf{I}_8\}$, are active in similar parts of the domain as $\{\mathbf{I}_1, \mathbf{I}_2\}$ and $\{\mathbf{I}_3, \mathbf{I}_4\}$, respectively, and have finer spatial structure compared with their annual counterparts.

c. *Connection between low-frequency and intermittent modes*

The intermittent modes have time series which appear to be a periodic mode modulated by a low-frequency signal. What low-frequency signal is modulating these modes? It turns out that most intermittent modes can be directly associated with a certain low-frequency mode from NLSA. Figure 6 shows time series snapshots for the annual and semiannual intermittent SST modes, I_1^{SST}, I_3^{SST}, I_5^{SST}, and I_7^{SST}, and low-frequency envelopes defined by L_1^{SST} (the PDO mode) and L_2^{SST} (the NPGO mode). We observe that I_3^{SST} and I_7^{SST} fit inside the NPGO envelope, and do not fit inside the PDO envelope. Similarly, I_1^{SST} and I_5^{SST} fit inside the PDO envelope and not the NPGO envelope. Despite clearly being modulated by a certain low-frequency mode, the intermittent modes are not simply products of a periodic mode and a low-frequency mode. The sea ice modes also share a similar relationship between the low frequency and intermittent modes. $\{I_1^{\text{ICE}}, I_2^{\text{ICE}}\}$, and $\{I_5^{\text{ICE}}, I_6^{\text{ICE}}\}$ are clearly modulated by L_1^{ICE} (the NPGO mode). $\{I_3^{\text{ICE}}, I_4^{\text{ICE}}\}$, and $\{I_7^{\text{ICE}}, I_8^{\text{ICE}}\}$ are not as clearly modulated by a certain low-frequency mode, but they are most closely associated with L_3^{ICE} (the PDO mode).

The intermittent modes have important phase relationships with their corresponding periodic modes. We find that the intermittent modes tend to either phase lock such that they are in phase or out of phase with the periodic mode, and this phase locking is determined by the sign of the low-frequency signal that modulates the intermittent mode. However, the intermittent modes also experience other phase relationships with the periodic modes, particularly during transitions between the two phase-locked regimes. In Fig. 7 we show three characteristic phase relationships between the intermittent and periodic modes. These plots, as well as the corresponding visualization in movie 2, show evolution of the intermittent modes $\{I_1^{\mathrm{ICE}}, I_2^{\mathrm{ICE}}\}$ in the $I_1^{\mathrm{ICE}} - I_2^{\mathrm{ICE}}$ complex plane (blue dots) and the periodic modes $\{P_1^{\mathrm{ICE}}, P_2^{\mathrm{ICE}}\}$ in the $P_1^{\mathrm{ICE}} - P_2^{\mathrm{ICE}}$ plane (red dots). The periodic modes trace a circle in the $P_1^{\mathrm{ICE}} - P_2^{\mathrm{ICE}}$ complex plane, and the intermittent modes trace out a more complicated trajectory. Also, plotted in cyan along the real axis is the value of L_1^{ICE}, the NPGO mode. We find that $\{I_1^{\mathrm{ICE}}, I_2^{\mathrm{ICE}}\}$ is in phase with $\{P_1^{\mathrm{ICE}}, P_2^{\mathrm{ICE}}\}$ when $L_1^{\mathrm{ICE}} > 0$ and out of phase when $L_1^{\mathrm{ICE}} < 0$. Finally, the green dot is the ratio of $\{I_1^{\mathrm{ICE}}, I_2^{\mathrm{ICE}}\}$ to $\{P_1^{\mathrm{ICE}}, P_2^{\mathrm{ICE}}\}$, where the ratio is taken by first writing these points in complex polar form. If $\{I_1^{\mathrm{ICE}}, I_2^{\mathrm{ICE}}\}$ were indeed the product of $\{P_1^{\mathrm{ICE}}, P_2^{\mathrm{ICE}}\}$ and L_1^{ICE}, we would expect this green dot to be perfectly coincident with the cyan dot for L_1^{ICE}. We observe that the intermittent mode is close to being a product of these two, yet is not an exact product (e.g., Fig. 7b). A similar phase behavior is observed for most other intermittent modes, but in some cases the near product relationship does not apply. For instance, $\{I_1^{\mathrm{SST}}, I_2^{\mathrm{SST}}\}$ are near products of $\{P_1^{\mathrm{SST}}, P_2^{\mathrm{SST}}\}$ and L_1^{SST}, but the corresponding ice modes, $\{I_3^{\mathrm{ICE}}, I_4^{\mathrm{ICE}}\}$, deviate significantly from the product of $\{P_1^{\mathrm{ICE}}, P_2^{\mathrm{ICE}}\}$ and L_3^{ICE}. In section 5 ahead, we will see that the phase relationships between the intermittent and periodic modes have important implications for explaining reemergence.

d. Comparison with SSA

In addition to NLSA, we also performed SSA on the coupled sea ice-SST dataset. These calculations were done by normalizing both variables to unit variance, and then performing SSA on the concatenated dataset. SSA produces periodic and low-frequency modes, and also two modes whose temporal patterns loosely resemble the intermittent modes of NLSA, with a broadband power spectrum around a certain base frequency and a bias towards lower frequencies. The periodic modes of SSA are very similar to the periodic modes of NLSA, but we observe a number of differences in the non-periodic modes. NLSA produces two low-frequency modes, which correlate strongly with the NPGO and PDO, respectively. SSA, on the other hand, produces a large number of low-frequency modes, most of which correlate most strongly with the PDO. For example, if we consider EOFs of North Pacific SST, we find that the leading eight low-frequency modes of SSA all correlate most strongly with the PDO (EOF 1). If we consider EOFs from the Northeast Pacific, we find that low-frequency modes 1, 2, 4, 5, 7, and 8 all correlate most strongly with the PDO (EOF 1) and modes 3 and 6 correlate most strongly with the NPGO (EOF 3). Low-frequency mode 3 has pattern correlations of 0.83 and 0.87 with the PDO and NPGO, respectively, and its spatial pattern looks like a mixed PDO-NPGO signal. The NLSA modes cleanly split low-frequency SST patterns between different modes, whereas SSA tends to mix these patterns over a large number of low-frequency modes. A consequence of this is that NLSA may be more effective at capturing patterns of variability using a small subset of modes. The two SSA modes that have a broadband power spectrum centered on a base frequency are different from the intermittent modes of NLSA in that their temporal patterns are not modulated by any of the the low-frequency SSA modes. Rather, these time series evolve independently of the other SSA modes. In the supplementary material, we present temporal patterns of selected SSA modes in Figure 1, and the spatiotemporal evolution of these modes in Movie 7.

We also performed NLSA on the unit variance dataset as a comparison with the phase velocity normalization presented above. We find three low-frequency modes, and pairs of annual and semiannual intermittent modes associated with these modes. A primary difference is that, unlike the phase velocity results above, the low-frequency modes do not cleanly split into patterns associated with the NPGO and PDO. Rather, low-frequency modes 1 and 2 correlate most strongly with the PDO (this is true for both North Pacific and Northeast Pacific EOFs). Low-frequency mode 3 has correlations of 0.81 and 0.89 with the PDO and NPGO (defined using Northeast Pacific EOFs), respectively, and has a spatial pattern that reflects a mixed NPGO-PDO signal. Preliminary results of NLSA on sea ice and sea level pressure indicate that the differences between unit variance normalization and the phase velocity approach may be more pronounced when one of the variables is significantly faster and noisier than the other.

5. Sea ice reemergence via NLSA

a. Sea ice reemergence in the North Pacific

Inspired by the sea ice reemergence mechanism put forward by BW, we study time lagged correlations of sea ice in the North Pacific sector of the ocean. We focus on the Bering and Okhotsk seas, the two primary areas of sea ice variability in the North Pacific. BW observe a spring-fall sea ice reemergence, in which sea ice anomalies of a certain sign in spring tend to produce anomalies of the same sign in the fall, despite lagged correlations dropping to near zero in the intervening summer months. The authors propose that spring sea ice anomalies create an anomaly of opposite sign in SST, and this SST imprint is retained over the summer months as the sea ice melts and the sea ice edge moves northwards. In the fall, the sea ice edge begins to move southward and when it reaches the SST anomaly it reinherits an ice anomaly of the same sign as the spring. It is by this proposed mechanism that SST stores the memory of melt season sea ice anomalies, allowing the same anomaly to be reproduced in the growth season.

b. Correlation methodology

BW compute time-lagged correlations for total arctic sea ice area as a method for examining sea ice reemergence. One drawback to this approach is that dynamically relevant spatial structures, such as sea ice dipoles, are integrated away when only considering total sea ice area. In order to capture the memory in sea ice spatial patterns, we perform time-lagged pattern correlations on the sea ice concentration data.

Specifically, we compute time lagged pattern correlations using the following methodology. First, we define $\bar{a}_m(x,y)$, the average sea ice concentration in a given month m, as a function of space. Let T be the number of samples of month m, and let m_k correspond to sample number $12(k-1)+m$, the mth month of the kth year. We set

$$\bar{a}_m(x,y) = \frac{\sum_{k=1}^{T} a_{m_k}(x,y)}{T}. \tag{4}$$

Next, we define the pattern correlation between times $m_k = 12(k-1)+m$ and $m'_j = 12(j-1)+m'$ as

$$P_{m_k m'_j} = \frac{\left\langle a_{m_k}(x,y) - \bar{a}_m(x,y), a_{m'_j}(x,y) - \bar{a}_{m'}(x,y) \right\rangle}{\|a_{m_k}(x,y) - \bar{a}_m(x,y)\| \|a_{m'_j}(x,y) - \bar{a}_{m'}(x,y)\|}. \tag{5}$$

In the above, $\langle \cdot, \cdot \rangle$ and $\| \cdot \|$ denote the Euclidean (area-weighted) inner product and two-norm with respect to the spatial gridpoints (x,y). Finally, we define the time lagged pattern correlation between months m and $m+\tau$ as the time average of all pattern correlations:

$$C_{m,m+\tau} = \frac{\sum_{k=1}^{T-2} P_{m_k m'_j}}{T-2}, \tag{6}$$

where $m_k = 12(k-1)+m$ and $m'_j = 12(j-1)+m' = m_k+\tau$. Note that time averaging is done over $T-2$ samples, because for lags up to 24 months there are only $T-2$ pairs of m_k and $m_k+\tau$.

c. Time lagged pattern correlations in the North Pacific sector

We compute time lagged pattern correlations in the North Pacific sector for all months and lags from 0 to 23 months, the results of which are shown in Fig. 8. In Fig. 8, the white boxes are not significant at the 95% level using a t–distribution statistic. All colored boxes are significant at the 95% level. Figure 8a shows time lagged total area correlations computed in the same way as BW, except being done for the North Pacific rather than the entire Arctic. We observe a similar correlation structure to that of BW, with one noteable difference. There is an initial decay of correlation over a 3–6 month timescale, after which, for the months of January–July, we observe an increase in correlation. This region of increased correlation is analogous to the "summer limb" of BW. In this summer limb, we can see natural pairings of spring months and the corresponding fall months in which the spring anomaly reemerges. These pairings are July-October, June-November, May-December, April-January, and March-January/February; they represent months at which the sea ice edge is similar in melt and growth seasons. A main difference between the North Pacific and the entire Arctic is that the North Pacific data does not contain a "winter limb" of anomalies produced in fall that are reproduced the following summer. This is because the North Pacific contains very little sea ice in the summer months. Figure 9 shows the monthly mean values plus/minus one standard deviation of North Pacific SST and sea ice concentration in the CCSM3 dataset. We see that the sea ice concentration is close to zero in the summer months and, moreover, there is significantly higher sea ice variability in high sea ice months.

Figure 8b shows lagged pattern correlations for North Pacific sea ice. As expected, the correlations are significantly weaker than in the total area lagged correlation case, since having a pattern correlation in anomalies is a much more stringent test than simply having correlations in total area of anomalies. Despite being weaker, the pattern correlations still have the "summer limb" structure observed in Fig. 8a, and these correlations are significant at the 95% level. Most lagged pattern correlations besides the inital decay and the summer limb are not significant at the 95% level. Figures 8c and 8d show lagged pattern correlations for the Bering (165°E – 160°W and 55° – 65°N) and Okhotsk (135°E – 165°E and 42° – 65°N) Seas, respectively. Each of these seas has a similar lagged pattern correlation structure to the full North Pacific sector in Fig. 8b.

Next, we seek to reproduce the lagged pattern correlations seen in the raw sea ice data using a low dimensional subset of coupled NLSA modes. We find that in each sea, a different set of modes is active, thus we choose to focus on the Bering and Okhotsk seas individually. In the Bering Sea, we find that modes $\{\mathbf{L}_1, \mathbf{I}_1, \mathbf{I}_2, \mathbf{I}_5, \mathbf{I}_6\}$ qualitatively reproduce the lagged pattern correlation structure seen in raw data. $\mathbf{L}_1$ is the NPGO mode and the other modes are the annual and semiannual intermittent modes which are modulated by the NPGO envelope. Moreover, this set appears to be the minimal subset, as smaller subsets of modes are unable to reproduce the correlation structure of the raw data. Figure 8e shows Bering Sea lagged pattern correlations computed using this three mode family, which we call the NPGO family. We see that this family has a very similar summer limb to the raw data, except with higher correlations, since this three–mode family decorrelates more slowly than the raw data.

Attempting a similar construction in the Okhotsk Sea, we find that modes $\{\mathbf{L}_2, \mathbf{I}_3, \mathbf{I}_4, \mathbf{I}_7, \mathbf{I}_8\}$ do the best job of reproducing the lagged pattern correlation structure. However, this mode family has clear deficiencies, as can be seen in Fig. 8f. In particular, this mode family fails to reproduce the summer decorrelation that is observed in the raw data and also has a less contiguous summer limb. $\mathbf{L}_2$ is the PDO mode and these intermittent modes are the annual and semiannual intermittent modes most closely associated to the PDO. Note that these intermittent modes are not perfectly modulated by the PDO, which may explain why this PDO family is unable to capture the sea ice reemergence signal as well as the NPGO family. Instead, in section 5f ahead we will see that this PDO family is more closely related to SST reemergence (Alexander et al. 1999)

Many other NLSA mode subsets were tested, but were unable to reproduce the correlation structure of the raw data as well as the subsets above. Also, the same procedure was performed using SSA modes, and it was found that small subsets of SSA modes (fewer than 25 modes) were unable to reproduce the lagged correlation structure of the raw data.

d. *A sea ice reemergence mechanism revealed through coupled NLSA*

Using the low-dimensional family of modes $\{\mathbf{L}_1, \mathbf{I}_1, \mathbf{I}_2, \mathbf{I}_5, \mathbf{I}_6\}$, active in the Bering Sea, to reconstruct patterns in the spatial domain, we observe sea ice and SST patterns which are remarkably consistent with the mechanism suggested by BW. Figure 10 shows the evolution of the three-mode family over the course of a year. These spatial patterns are composites, obtained by averaging over all years in which the NPGO is active in its positive phase (defined as $L_2^{\text{SST}} > 1.5$). A very similar spatiotemporal pattern, with opposite sign, occurs in years when the NPGO is active in its negative phase. The dynamic evolution of this three-mode family is shown in movie 3. In January, there is a positive sea ice anomaly and a negative SST anomaly in the southern part of the Bering Sea. The main SST anomaly extends slightly further south than the sea ice anomaly, and there is also a weaker negative anomaly extending southward and eastward in the domain. The positive ice anomalies continue to move southward through the growth season, until reaching the maximum ice extent in March. The SST anomaly has not changed significantly from January and is primarily localized to the ice anomaly region. In particular, there is no SST anomaly in the northern part of the Bering Sea. The melt season begins in April, and in May we observe that the sea ice anomaly has moved northward. The SST anomaly has also extended northward while maintaing its southern extent from March. In July the sea ice retreats further and only a weak positive anomaly remains in the Bering Sea. By September essentially no sea ice anomaly remains in the Bering Sea. Despite the sea ice anomaly being absent in September, the SST has a strong negative anomaly throughout the entire Bering Sea region. The northern Bering sea, previously free of SST anomalies, now has a negative anomaly, imprinted by the positive sea ice anomalies moving through the region during the melt season. As the sea ice returns to the domain in October–December, the ice interacts with the SST anomaly, using the cold SST to grow additional ice, and reproduces the positive ice anomaly that we observed in the spring. In November, part of the northern Bering Sea's negative SST anomaly has been wiped out, and the ice has begun to redevelop its positive anomaly. The ice continues to grow stronger positive anomalies as it moves southward and in January the cycle roughly repeats again. We observe this mechanism with the NPGO mode in both positive and negative phase.

As could be expected from Fig. 8f, the mode family $\{\mathbf{L}_2, \mathbf{I}_3, \mathbf{I}_4, \mathbf{I}_7, \mathbf{I}_8\}$ does not have a clear sea ice reemergence in the Okhotsk Sea. This family does exhibit a winter-winter persistence of ice anomalies, but the anomalies tend to unrealistically persist over the intervening summer months.

e. Reemergence conditioned on low-frequency modes

We earlier noted that the NPGO mode family $\{\mathbf{L}_1, \mathbf{I}_1, \mathbf{I}_2, \mathbf{I}_5, \mathbf{I}_6\}$ is able to reproduce the lagged correlation structure seen in sea ice data in the Bering Sea. Additionally, we know that the intermittent modes within the mode families identified here are modulated by the low-frequency mode of that family. Thus, in order to determine whether a given mode family is active, we can simply assess whether or not the corresponding low–frequency mode is active. Given these observations, one would expect to see an enhanced reemergence structure if we performed lagged correlations on the raw sea ice data, conditional on a certain low-frequency mode being active. Indeed, if we condition on the NPGO being active, we observe an enhanced summer limb in the lagged pattern correlation structure of the Bering Sea raw data. Similarly, if we condition on the NPGO being inactive, we find that the summer limb is significantly weakened. Figure 11 shows conditional lagged pattern correlations for these various cases. Note that the NPGO is defined as "active" over the time interval $[t, t + \Delta t]$ if $|L_2^{\mathrm{SST}}| > 1.5$. The NPGO index is defined for $t \in [1, s - q]$.

This summer limb strengthening has implications for regional sea ice predictibility. In particular, tracking the NPGO index should help one predict whether a given spring anomaly in the Bering sea will return the following fall.

f. *Connection to other reemergence phenomena*

BW also note a summer-to-summer reemergence in Arctic sea ice, which is connected to persistence in sea ice thickness anomalies. This summer-to-summer reemergence is not seen in the North Pacific sector, since the North Pacific is essentially sea ice free for the months of July through October (see Fig. 9).

Another reemergence phenomenon active in the North Pacific sector is the winter-to-winter SST reemergence studied by Alexander et al. (1999). This reemergence consists of the formation of an SST anomaly in winter months, a weakening of the anomaly over the summer due to the presence of a seasonal thermocline, and a subsequent re-strengthening the following winter. To investigate the presence of SST reemergence in the coupled NLSA modes, we perform a lagged correlation analysis analogous to the sea ice study above.

We focus on the domains of active SST reemergence defined by Alexander et al. (1999): the central ($26° - 42°$N, $164° - 148°$W), eastern ($26° - 42°$N, $132° - 116°$W), and western ($38° - 42°$N, $160° - 180°$E) Pacific. For each of these domains, time lagged pattern correlations of SST were computed, including conditioning on certain low-frequency SST modes being active. It was found that correlations were significantly strengthened when the PDO mode ($\mathbf{L}_2$) was active, and were relatively unaffected by the state of the NPGO mode ($\mathbf{L}_1$). Figure 12 shows time-lagged pattern correlations for the central, eastern, and western Pacific domains, for both the raw SST data, and the raw SST data conditioned on an active PDO. In the central and eastern parts of the basin, we observe a strengthened reemergence signal when the PDO is active, as there is a clear drop in correlation over the summer months and a significantly stronger increase in correlation the following winter. In the western part of the basin, the reemergence signal is clear without any PDO conditioning. With an active PDO, the correlations become stronger, and the summer decorrelation remains visible. Note that, unlike North Pacific sea ice reemergence, the SST correlations do not vanish over the summer months. Rather, they simply weaken over the summer and re-strengthen the following winter.

Following the sea ice approach above, we seek a low-dimensional family of NLSA modes that reflect the lagged correlation structure of the raw data. We find that the PDO mode family, $\{\mathbf{L}_2, \mathbf{I}_3, \mathbf{I}_4, \mathbf{I}_7, \mathbf{I}_8\}$, has the highest skill in reproducing the observed correlations. Figure 13 shows a composite reconstruction of the SST patterns of the PDO family, where the composite is taken over years where the PDO index is high ($L_1^{\mathrm{SST}} > 1.5$). SST reemergence is most strikingly observed in the central Pacific. We observe a strong negative SST anomaly in January and March, which begins to decay in May, and is significantly weaker, yet still positive, in September. The anomaly begins to strengthen in November, and the pattern roughly repeats again the following year. As could be expected by the lagged correlations, we observe stronger SST persistence in the western Pacific, however a summer weakening and winter re-strengthening is nonetheless visible. The anomaly strength is significantly smaller in the eastern Pacific domain, but a similar SST reemergence with positive anomalies can be observed, though the signal is poorly represented with the colorbar of Fig. 13 (chosen for the entire North Pacific). Note that there is also an active SST reemergence with positive anomalies along the Alaska-British Columbia coastline. When the PDO is active in its negative phase, a similar pattern is observed, with opposite sign. The dynamic evolution of the PDO mode family is shown in Movie 4. An interesting topic of future study would be to investigate whether the vertical structure of this reemergence mechanism can be captured by a low dimensional family of NLSA modes.

6. Comparison with Observations

a. Coupled NLSA on a short time series

To this point, all results have been derived from analysis of a 900-yr CCSM3 model integration. Given the relative shortness of most observational climate time series, a natural question is whether the coupled NLSA approach can be applied to a shorter time series for the purposes of exploratory data analysis. Given that NLSA is based upon sufficient exploration of a high-dimensional manifold, a short observational time series provides a stringent test for the algorithm. Nevertheless, it is plausible that certain coarse-grained nonlinear geometric features are adequately sampled (in particular, the periodic dimension associated with the seasonal cycle, which is crucial for reemergence). To test the feasibility of NLSA in this environment, we studied the HADISST dataset, which consists of 34 years of satellite observations of sea ice and SST.

We performed coupled NLSA on the HADISST dataset in a completely analogous manner to the CCSM3 results above, using a value of $\epsilon = 0.8$, a truncation level of $l = 22$, and a lagged embedding window of $\Delta t = 24$ months. The resulting temporal modes have very similar characteristics to the temporal modes of the CCSM3 dataset, cleanly splitting into periodic, low-frequency and intermittent modes. We find that the periodic and intermittent modes come in doubly degenerate pairs, and that each intermittent mode is modulated by a certain low-frequency mode. Also, we find that each SST PC is highly correlated with a certain sea ice PC, motivating the definition of coupled sea ice-SST modes of variability. For the sake of brevity, we only define the coupled modes that will be discussed in the following sections: $\mathbf{L}_1 = (L_1^{\text{ICE}}, L_2^{\text{SST}})$, $\mathbf{L}_2 = (L_2^{\text{ICE}}, L_1^{\text{SST}})$, $\mathbf{I}_1 = (I_1^{\text{ICE}}, I_4^{\text{SST}})$, $\mathbf{I}_2 = (I_2^{\text{ICE}}, I_3^{\text{SST}})$, $\mathbf{I}_3 = (I_3^{\text{ICE}}, I_2^{\text{SST}})$, $\mathbf{I}_4 = (I_4^{\text{ICE}}, I_1^{\text{SST}})$, $\mathbf{I}_5 = (I_5^{\text{ICE}}, I_7^{\text{SST}})$, $\mathbf{I}_6 = (I_6^{\text{ICE}}, I_8^{\text{SST}})$, $\mathbf{I}_7 = (I_7^{\text{ICE}}, I_5^{\text{SST}})$, $\mathbf{I}_8 = (I_8^{\text{ICE}}, I_6^{\text{SST}})$. Time series snapshots, autocorrelation functions, and power spectral densities for the leading low-frequency ice modes and an annual and semiannual intermittent mode are shown in Figure 14.

Similar to the CCSM3 results, the spatial patterns of these modes have correspondences with the NPGO and PDO. We find that $\mathbf{L}_1$ has a maximum pattern correlation of 0.65 with EOF 2 of Northeast Pacific SST, and $\mathbf{L}_2$ has a maximum pattern correlation of 0.90 with EOF 1 of North Pacific SST. Note that these EOFs were computed using SST output of HADISST. In light of these correlations, we call $\mathbf{L}_1$ the NPGO mode and $\mathbf{L}_2$ the PDO mode.

The sea ice patterns of these modes have some notable differences from their CCSM3 counterparts. $\mathbf{L}_1$ has strong sea ice anomalies in the Bering Sea, but also has strong anomalies of the opposite sign in the Sea of Okhotsk. This pattern of sea ice variability is consistent with the leading sea ice EOF found in Deser et al. (2000) and Liu et al. (2007). $\mathbf{L}_2$ consists of a strong sea ice anomaly throughout the Okhotsk Sea, and also an anomaly of the same sign in the southern part of the Bering Sea. Each of these low-frequency modes modulates a pair of annual and a pair of semiannual intermittent modes. These intermittent modes are active in similar parts of the domain as the low-frequency modes, and have finer spatial structures, as we also observed with the CCSM3 results.

b. Sea ice reemergence in observations

With these coupled observational modes at our disposal, we now investigate North Pacific sea ice reemergence in the observational record. First, we compute time lagged pattern correlations in the North Pacific sector, shown in Fig. 15a. We observe that there is no reemergence signal visible in these correlations. This is also the case for correlations computed over the Bering and Okhotsk Seas individually. Despite the lack of reemergence in the observational data, we examine a number of NLSA mode subsets for the presence of a reemergence signal. We find the strongest signal with the mode family $\{\mathbf{L}_1, \mathbf{I}_1, \mathbf{I}_2, \mathbf{I}_5, \mathbf{I}_6\}$, where the correlations are computed over the Bering Sea. The correlations are shown in Fig. 15b. This family also has signs of a reemergence signal in the Okhotsk Sea, except that the ice anomalies anti-correlate over the summer months, instead of simply decorrelating. Does this mode family have any explanatory power with regards to sea ice reemergence? The answer appears to be yes. Fig. 15c shows North Pacific lagged pattern correlations, conditional on the NPGO mode, $\mathbf{L}_1$, being active. We observe an emphasized reemergence limb in years when the NPGO mode is active. A similar appearance of a summer limb is observed in the Bering Sea, but not in the Okhotsk, when conditioning on an active NPGO.

A sea ice-SST reconstruction for the year 2001, using the mode family $\{\mathbf{L}_1, \mathbf{I}_1, \mathbf{I}_2, \mathbf{I}_5, \mathbf{I}_6\}$, is shown in Figure 16. This family shares some similarities to the NPGO mode family found in CCSM3, with the NPGO mode modulating the annual and semiannual intermittent modes, but also has many clear differences. In the winter months, we observe strong sea ice anomalies of opposite sign in the Bering and Okhotsk seas. The Okhotsk anomalies were not present in the CCSM3 results. Spatially coincident with these ice anomalies, we observe SST anomalies of the opposite sign. We also observe strong SST anomalies throughout most of the North Pacific basin, especially along the Kuroshio extension region. This is different from the CCSM3 results, in which the SST anomalies of the NPGO family were primarily contained in the northern portion of the domain. During the months of July–October the Bering and Okhotsk Seas are relatively ice free, and we observe persistence of SST anomalies of opposite sign to the ice anomalies. Compared to CCSM3 results, the summer SST anomalies do not cover the Bering Sea as completely; there is a portion of the northwest Bering sea that remains anomaly-free over the summer. In the late fall and early winter, sea ice anomalies reappear in the Bering and Okhotsk seas, adopting the same sign they had the previous winter. This cycle roughly repeats itself the following winter. This family reflects the same SST-sea ice reemergence mechanism as seem in CCSM3, albeit in a slightly less clean manner.

Why is the North Pacific sea ice reemergence signal significantly stronger in CCSM3 than in observations? One possibility is that the CCSM3 model overemphasizes the winter-to-winter persistence of the ice and SST anomalies associated with the NPGO. Another possibility is that the raw observational data, after linear detrending, contains a residual signal associated with a nonlinear trend. This nonlinear trend may act to obscure the reemergence signal in the raw data, though we find that the reemergence signal is sufficiently strong to be recoverable in the NPGO-conditioned data. Yet another possibility is that over the relatively short observational record, the low-frequency NPGO mode has been generally inactive, and a longer time series would reveal the reemergence signal.

To investigate the latter possibility, we divided the 900-year CCSM3 record into a number of 34 year datasets, analogous to the length of the observational record, and performed lagged correlations on each of these short timeseries. We found significant variation in the sea ice reemergence signal over these different datasets, including some sets where the reemergence signal was absent, much like in observations. There were other 34 year datasets which contained a much stronger reemergence limb, quite similar to the conditional lagged correlations of Fig. 11b. Therefore, it is plausible that the record of satellite observations is simply too short to provide a sufficient sampling of low-frequency variability of the coupled ocean-sea ice system, and correlations computed using this dataset may not fully reflect the intrinsic variability of this system. We also computed lagged correlations of the sea ice observations in other parts of the Arctic Ocean, and found strong reemergence signals in the Barents and Kara Seas, the Labrador Sea, and the Greenland Sea.

c. SST reemergence in observations

We also investigate SST reemergence in the HADISST dataset by computing time lagged pattern correlations in the North Pacific. Fig. 17a shows lagged correlations of the raw SST data and Fig. 17b shows lagged correlations conditional on the PDO mode, $\mathbf{L}_2$, being active. We observe a strengthened winter-to-winter SST reemergence when the PDO is active. We also conditioned on other low-frequency modes, and found that the PDO produces the most prominent strengthening of correlation. Note that these correlations are computed over the entire North Pacific domain, rather than the smaller domains considered in section 5f. This choice was made because the conditional correlations were quite noisy when performed over the smaller domains, since the PDO is only "active" for about 25% of the observational record.

The coupled NLSA observational modes also have a mode family $\{\mathbf{L}_2, \mathbf{I}_3, \mathbf{I}_4, \mathbf{I}_7, \mathbf{I}_8\}$, which is analogous to the PDO family of CCSM3. In Fig. 18 we show an SST reconstruction for the year 2005 using this mode family. We observe an active SST reemergence in the central and eastern Pacific domains, but there is not a clear reemergence in the western Pacific. The reemergence in the central and eastern Pacific happens at different times of year, with weakest anomalies in September and November, respectively. Similar to the CCSM3 results, the observational PDO family has a large-scale anomaly along the Kuroshio extension region, and significant variability in the central Pacific. A primary difference is that the observational PDO family has much stronger anomalies along the west coast of North America than the PDO family of CCSM3.

7. Conclusions

In this work, we have studied reemergence mechanisms for North Pacific sea ice in comprehensive climate model output and in satellite observations. We have introduced a new modification to the NLSA algorithm for high-dimensional time series (Giannakis and Majda 2013, 2012c), which allows for a scale-invariant coupled analysis of multiple variables in different physical units. This algorithm computes a kernel matrix using the individual phase space velocities for each variable, simultaneously removing physical units from the analysis, as well as implicitly selecting the variance ratio between the two variables. This coupled NLSA algorithm was applied to North Pacific SST and sea ice concentration data from a 900 year CCSM3 control integration, and a set of temporal patterns, analogous to PCs, and spatiotemporal patterns, analogous to extended EOFs, were obtained. The same analysis was performed on the 34 year record of sea ice and SST satellite observations. The modes recovered by coupled NLSA include periodic and low-frequency patterns of variability of sea ice and SST, as well as intermittent patterns not captured by SSA. The leading low-frequency modes correlate well with the familiar PDO and NPGO patterns of North Pacific SST variability. The intermittent modes have a base frequency of oscillation and are modulated by either the PDO or NPGO low-frequency signal, and tend to either be in phase or out of phase with their corresponding periodic cycle.

Using the modes obtained via coupled NLSA, we investigated the phenomenon of sea ice reemergence suggested by BW, in the North Pacific region. In the CCSM3 data, it was found that the raw sea ice data of the North Pacific exhibited a similar reemergence of correlation to that seen by BW, a noteable difference being the lack of a "winter limb." Seeking a low-dimensional family of modes to explain this reemergence process, we found that the NPGO and its corresponding annual and semiannual intermittent modes were able to reproduce the lagged correlations seen in the Bering Sea. Moreover, reconstructing patterns in the spatial domain, we found that this low-dimensional family demonstrates a sea ice reemergence mechanism, in which summer SST stores the memory of springtime sea ice anomalies, remarkably well. It was also found that conditioning the raw sea ice data on the NPGO being active, led to a significantly strengthened "summer limb" in the lagged correlations of the Bering Sea, which has implications for regional predictability of sea ice reemergence. Also, the family of NLSA modes related to the PDO was able capture a winter-to-winter reemergence of SST anomalies, both in lagged correlations and in spatial reconstructions.

The raw observational sea ice record does not contain a sea ice reemergence signal in the North Pacific sector. However, when conditioned on the NPGO mode being active, a clear summer limb appears in the raw data lagged correlations. Additionally, an analogous NPGO family exists for the observations, and displays a similar SST-sea ice reemergence mechanism. An enhanced winter-to-winter SST reemergence was found when conditioning on an active PDO. Also, the observational modes have a PDO family, which exhibits SST reemergence in the North Pacific. In future work, we plan to add North Pacific sea level pressure to our coupled analysis to gain insight into the variability of the coupled atmosphere-sea ice-ocean system.

Acknowledgments.

We would like to thank two anonymous reviewers for their valuable comments and suggestions. The authors would like to acknowledge the support of ONR MURI grant 25-74200-F7112 and ONR DRI grant N00014-14-1-0150. M. Bushuk was supported by the NYU Abu Dhabi Research Institute, under project G1204, and by NSERC PGS-D award 404213. We would also like to thank David Holland for helpful discussions.

REFERENCES

Alexander, M. A., C. Deser, and M. S. Timlin, 1999: The reemergence of SST anomalies in the North Pacific Ocean. *J. Climate*, **12**, 2419–2433.

Blanchard-Wrigglesworth, E., K. C. Armour, C. M. Bitz, and E. DeWeaver, 2011: Persistence and inherent predictability of Arctic sea ice in a GCM ensemble and observations. *J. Climate*, **24**, 231–250.

Broomhead, D. S. and G. P. King, 1986: Extracting qualitative dynamics from experimental data. *Phys. D*, **20 (2–3)**, 217–236, doi:10.1016/0167-2789(86)90031-x.

Budyko, M., 1969: The effect of solar radiation variations on the climate of the earth. *Tellus*, **21**, 611–619.

Cavalieri, D. J. and C. L. Parkinson, 1987: On the relationship between atmospheric circulation and the fluctuations in the sea ice extents of the Bering and Okhotsk Seas. *J. Geophys. Res.*, **92(C7)**, 7141–7162.

Coifman, R. R. and S. Lafon, 2006: Diffusion maps. *Appl. Comput. Harmon. Anal.*, **21(1)**, 5–30, doi:10.1016/j.acha.2006.04.006.

Collins, W. D., et al., 2006: The Community Climate System Model version 3 (CCSM3). *J. Climate*, **19**, 2122–2143.

Curry, J. A., J. L. Schramm, and E. E. Ebert, 1995: Sea ice-albedo climate feedback mechanism. *J. Climate*, **8**, 240–247.

Deser, C., J. E. Walsh, and M. S. Timlin, 2000: Arctic sea ice variability in the context of recent atmospheric circulation trends. *J. Climate*, **13**, 617–633.

Di Lorenzo, E., et al., 2008: North Pacific Gyre Oscillation links ocean climate and ecosystem change. *Geophys. Res. Lett*, **35**, L08 607, doi:10.1029/2007GL032838.

Fang, Z. and J. Wallace, 1994: Arctic sea ice variability on a timescale of weeks and its relation to atmospheric forcing. *J. Climate*, **7**, 1897–1914.

Ghil, M., et al., 2002: Advanced spectral methods for climatic time series. *Rev. Geophys.*, **40(1)**, 3.1–3.41.

Giannakis, D., 2014: Dynamics-adapted cone kernels. *SIAM J. Appl. Dyn. Sys.*, submitted.

Giannakis, D. and A. J. Majda, 2012a: Comparing low-frequency and intermittent variability in comprehensive climate models through nonlinear Laplacian spectral analysis. *Geophys. Res. Lett*, **39**, L10 710, doi:10.1029/2012GL051575.

Giannakis, D. and A. J. Majda, 2012b: Limits of predictability in the North Pacific sector of a comprehensive climate model. *Geophys. Res. Lett*, **39**, L24 602, doi:10.1029/2012GL054273.

Giannakis, D. and A. J. Majda, 2012c: Nonlinear Laplacian spectral analysis for time series with intermittency and low-frequency variability. *Proc. Natl. Acad. Sci.*, **109**, 2222–2227.

Giannakis, D. and A. J. Majda, 2013: Nonlinear Laplacian spectral analysis: Capturing intermittent and low-frequency spatiotemporal patterns in high-dimensional data. *Stat. Anal. Data Min.*, **6 (3)**, 180–194, doi:10.1002/sam.11171.

Giannakis, D. and A. J. Majda, 2014: Data-driven methods for dynamical systems: Quantifying predictability and extracting spatiotemporal patterns. *Mathematical and Computational Modeling: With Applications in Engineering and the Natural and Social Sciences*, R. Melnik, Ed., Wiley, Hoboken, 288.

Holland, M. M., C. Bitz, E. Hunke, W. Lipscomb, and J. Schramm, 2006: Influence of the sea ice thickness distribution on polar climate in CCSM3. *J. Stat. Phys.*, **19**, 2398–2414.

Liu, J., Z. Zhang, R. M. Horton, C. Wang, and X. Ren, 2007: Variability of North Pacific sea ice and East Asia-North Pacific winter climate. *J. Climate*, **20**, 1991–2001.

Mantua, N. J. and S. Hare, 2002: The Pacific Decadal Oscillation. *J. Oceanogr.*, **58**, 35–44, doi:10.1023/A:1015820616384.

Parkinson, C. L., 1990: The impacts of the Siberian high and Aleutian low on the sea ice cover of the Sea of Okhotsk. *Ann. Glaciology*, **14**, 226–229.

Rayner, N. A., D. E. Parker, E. B. Horton, C. K. Folland, L. V. Alexander, D. P. Rowell, E. C. Kent, and A. Kaplan, 2003: Global analyses of sea surface temperature, sea ice, and night marine air temperature since the late nineteenth century. *J. Geophys. Res.*, **108**, 4407, doi:10.1029/2002JD002670.

Sasaki, Y. N. and S. Minobe, 2006: Seasonally dependent interannual variability of sea ice in the Bering Sea and its relation to atmospheric fluctuations. *J. Geophys. Res.*, **110**, C05 011.

Smith, R. and P. Gent, 2004: Reference manual for the Parallel Ocean Program (POP): Ocean component of the Community Climate System Model (CCSM2.0 and 3.0). Tech. Rep. LAUR-02-2484, Los Alamos National Laboratory, 75 pp.

Teng, H. and G. Branstator, 2011: Initial value predictability in prominent modes of North Pacific subsurface temperature in a coupled GCM. *Climate Dyn.*, **36**, 1813–1834.

Vautard, R. and M. Ghil, 1989: Singular spectrum analysis in nonlinear dynamics, with applications to paleoclimatic time series. *Phys. D*, **35**, 395–424, doi:10.1016/0167-2789(89) 90077-8.

Walsh, J., 1983: The role of sea ice in climatic variability: Theories and evidence. *Atmos.-Ocean*, **21**, 229–242.

List of Figures

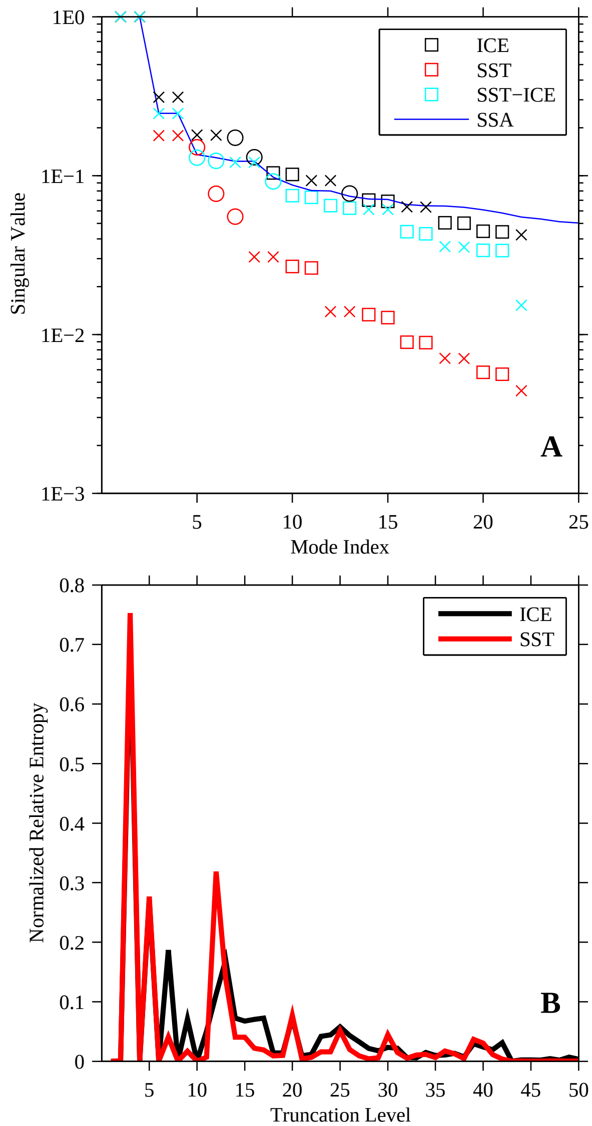

FIG. 1. (a) Singular values from coupled NLSA with phase velocity normalization (black and red markers show ice and SST singular values, respectively), variance normalization (cyan markers), and SSA (blue line). The singular values have been normalized so that $\sigma_1 = 1$. Low-frequency modes are indicated by "◯", periodic modes by "×", and intermittent modes by "□". (b) Normalized relative entropy for A_l^{ICE} and A_l^{SST} vs truncation level l. Spikes in the relative entropy curve indicate possible candidates for the choice of truncation level.

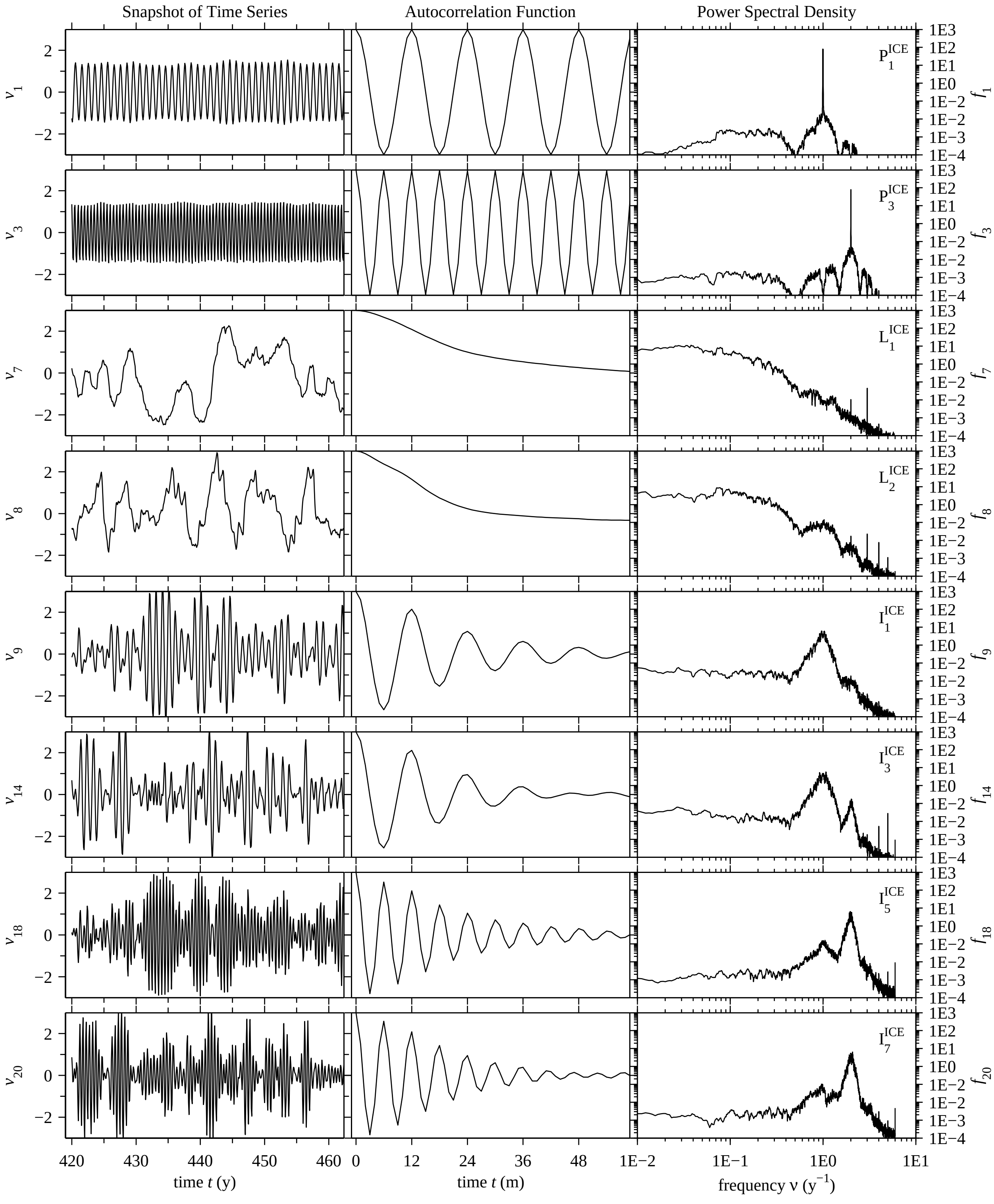

FIG. 2. Snapshots of the time series, power spectral density, and autocorrelation functions for the sea-ice PCs (v_k) from coupled NLSA. Shown here are the annual periodic (P_1^{ICE}) and semiannual periodic (P_3^{ICE}) modes, the NPGO mode (L_1^{ICE}), the PDO mode (L_2^{ICE}), annual intermittent modes (I_1^{ICE} and I_3^{ICE}), and semiannual intermittent modes (I_5^{ICE} and I_7^{ICE}). The autocorrelation vertical scale is [-1,1]. The power spectral densities (f_k) were estimated over the full 900 year timeseries via the multitaper method with time-bandwidth product $p = 6$ and $K = 2p - 1 = 11$ Slepian tapers.

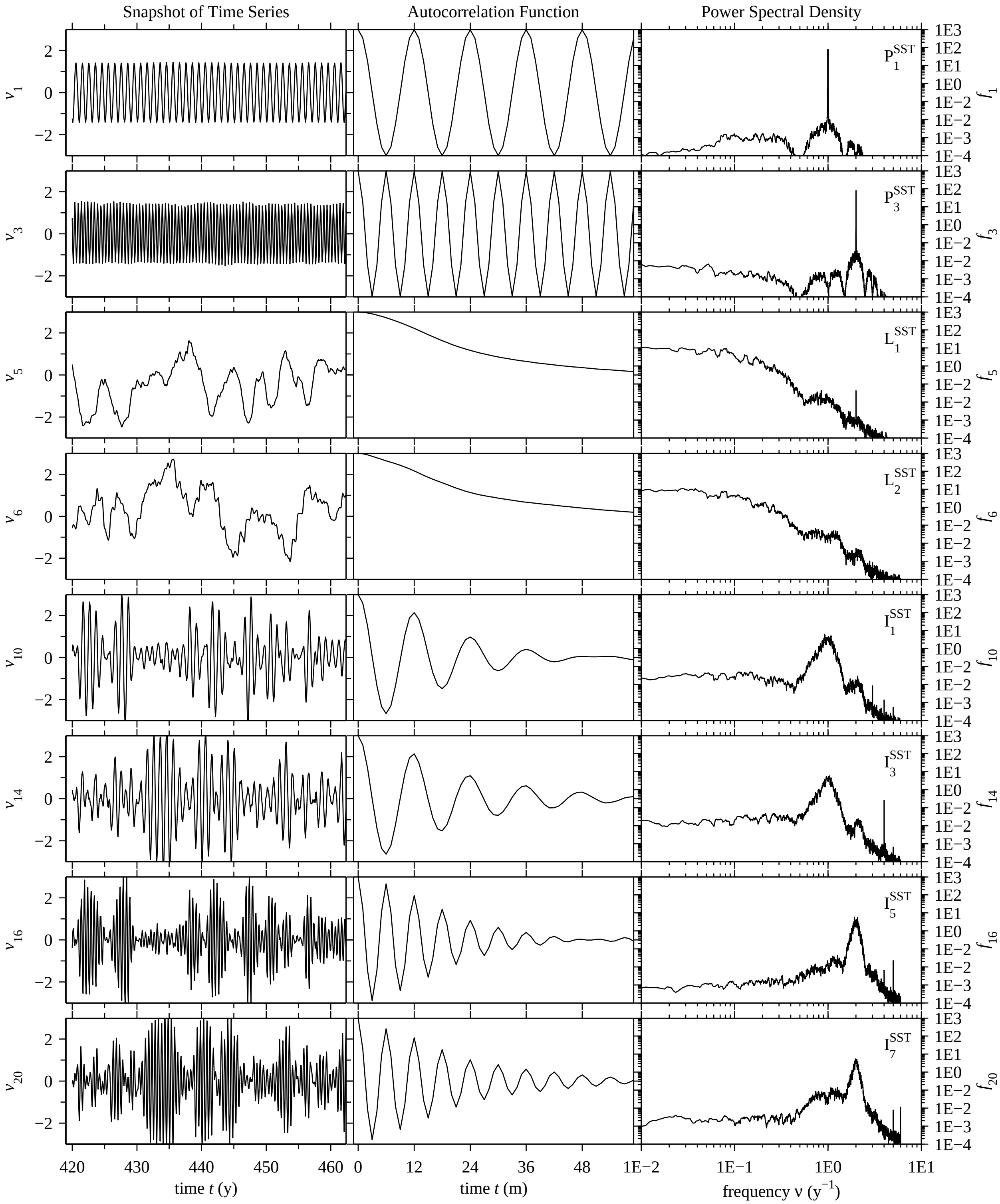

FIG. 3. Snapshots of the time series, power spectral density, and autocorrelation functions for the SST PCs (v_k) from coupled NLSA. Shown here are the annual periodic (P_1^{SST}) and semiannual periodic (P_3^{SST}) modes, the PDO mode (L_1^{SST}), the NPGO mode (L_2^{SST}), annual intermittent modes (I_1^{SST} and I_3^{SST}), and semiannual intermittent modes (I_5^{SST} and I_7^{SST}). The autocorrelation vertical scale is [-1,1]. The power spectral densities (f_k) were estimated over the full 900 year timeseries via the multitaper method with time-bandwidth product $p = 6$ and $K = 2p - 1 = 11$ Slepian tapers.

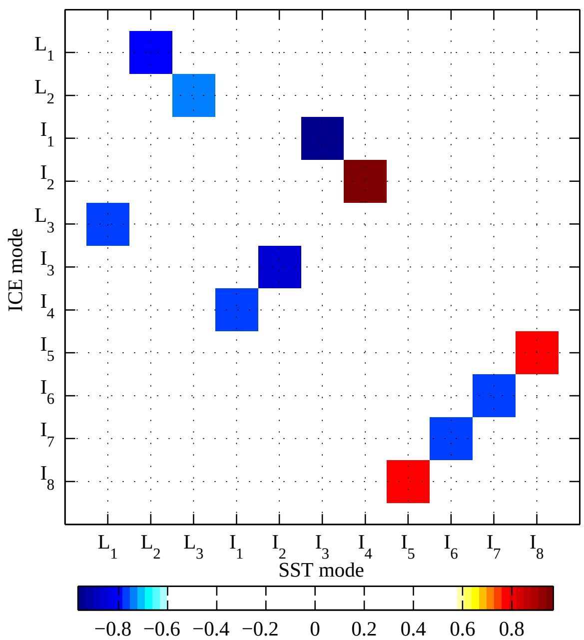

Fig. 4. Correlations between selected SST and and sea ice principal components. Note that each SST PC can be associated with a single sea ice PC.

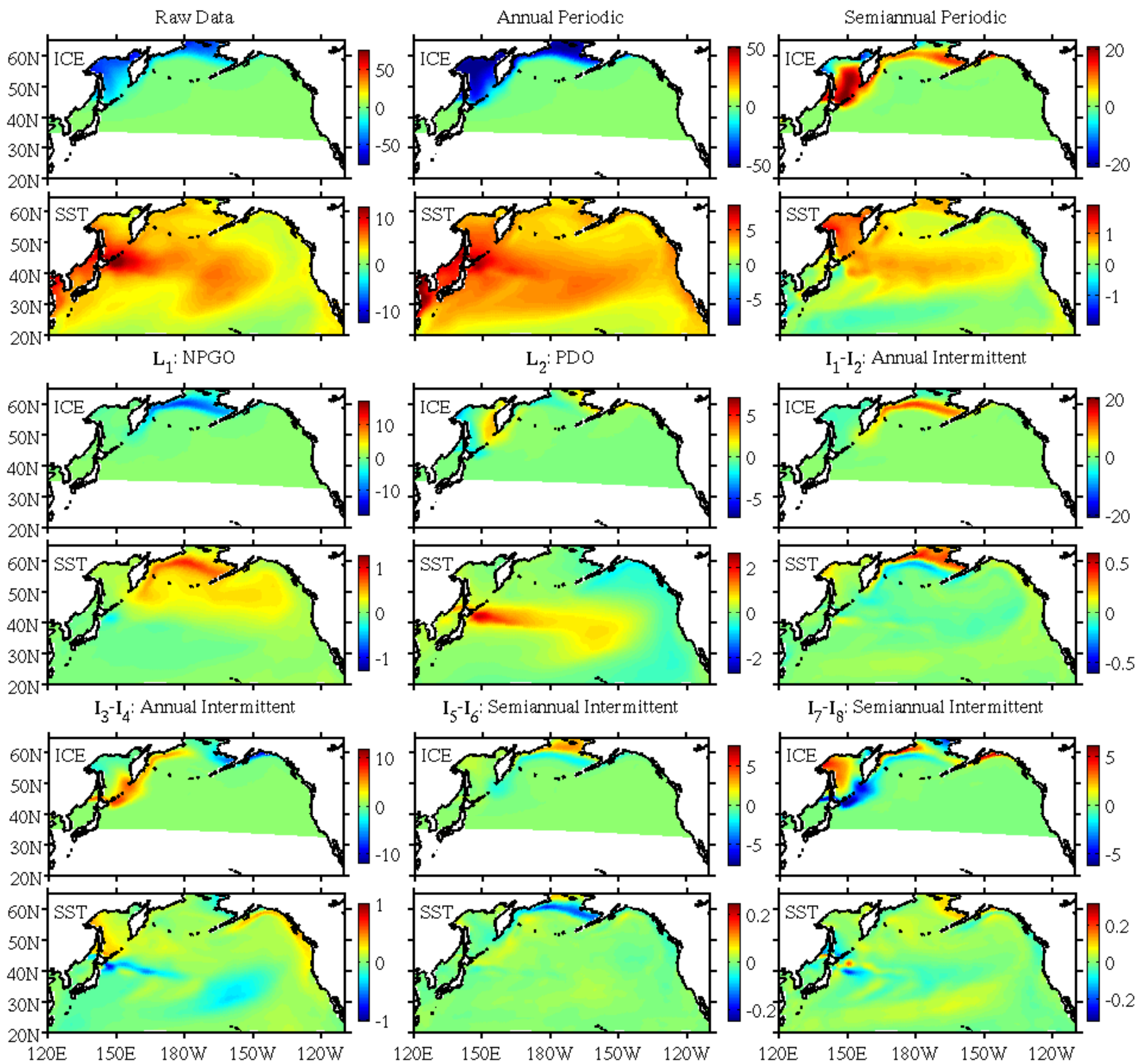

FIG. 5. Snapshots of raw data and spatiotemporal modes from coupled NLSA. See movie 1 for the dynamic evolution of these modes.

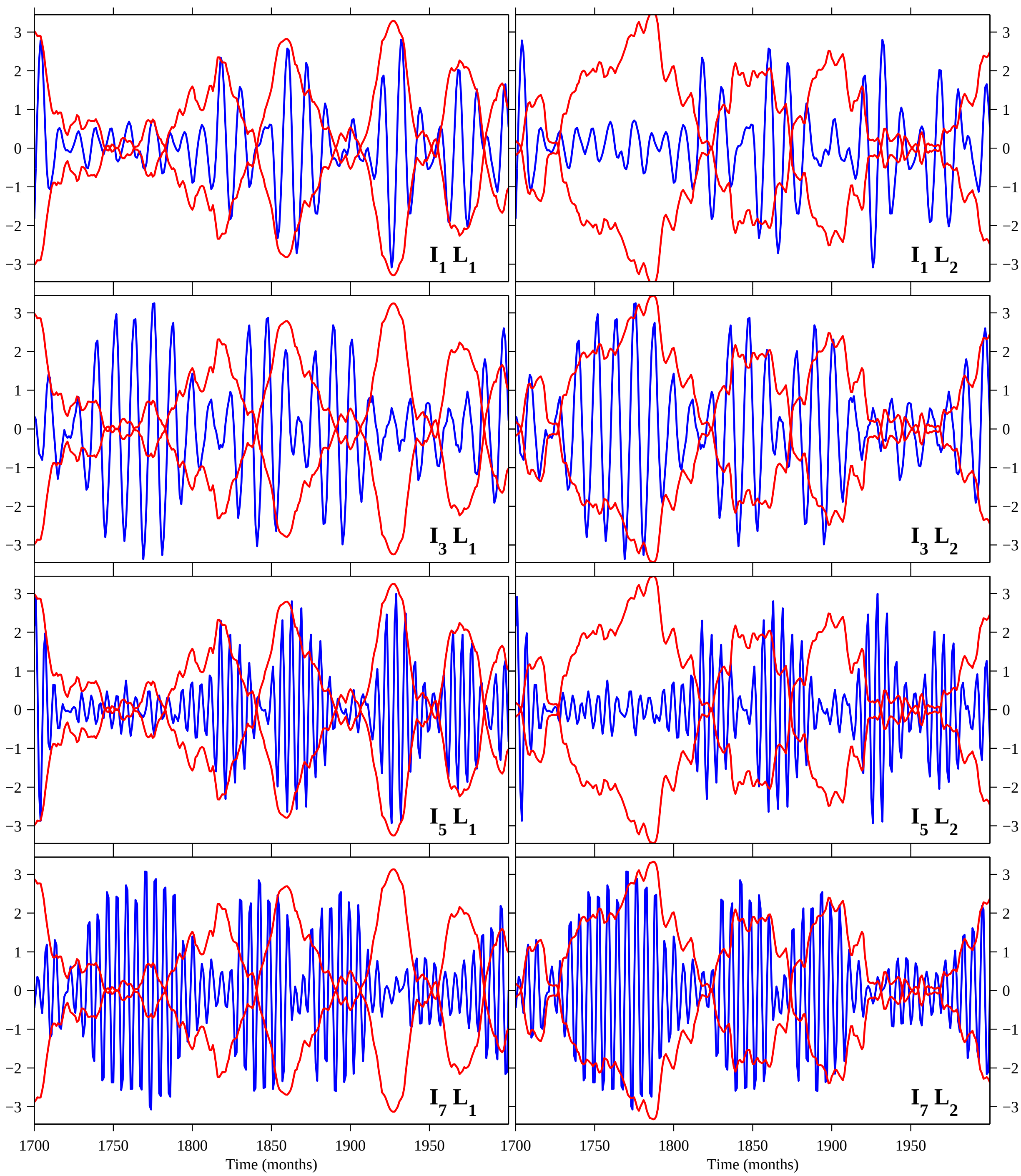

FIG. 6. Time series of intermittent modes $I_1^{\rm SST}, I_3^{\rm SST}, I_5^{\rm SST}, I_7^{\rm SST}$ plotted in blue, and low-frequency envelopes defined by $L_1^{\rm SST}$ (PDO) and $L_2^{\rm SST}$ (NPGO) plotted in red.

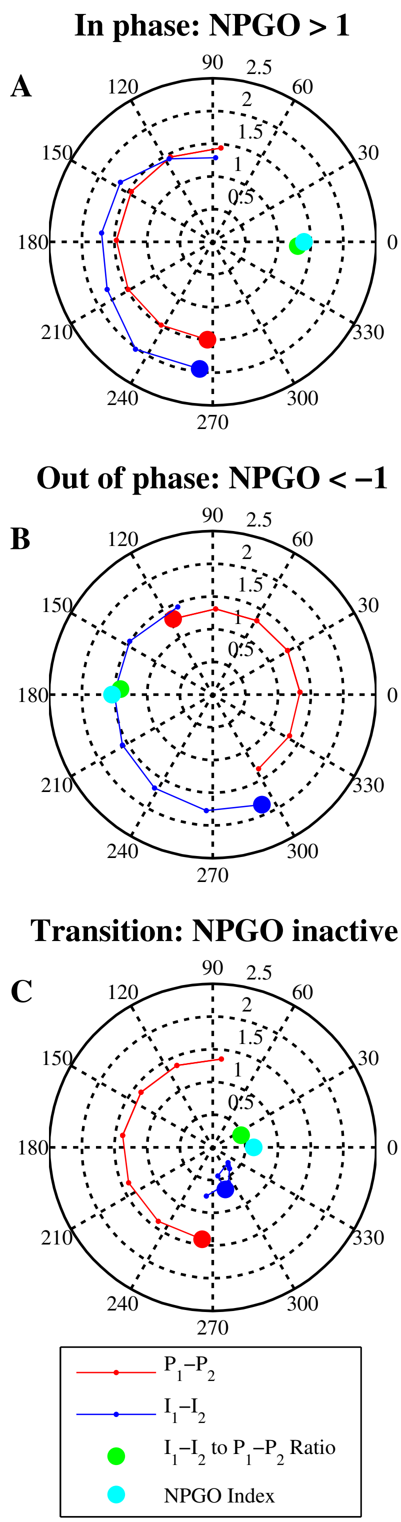

FIG. 7. Phase evolution of intermittent modes $\{I_1^{\mathrm{ICE}}, I_2^{\mathrm{ICE}}\}$ in the $I_1^{\mathrm{ICE}} - I_2^{\mathrm{ICE}}$ plane (blue dots) and periodic modes $\{P_1^{\mathrm{ICE}}, P_2^{\mathrm{ICE}}\}$ in the $P_1^{\mathrm{ICE}} - P_2^{\mathrm{ICE}}$ plane (red dots), where the present value is shown with the larger dot and the smaller dots show the previous six values. The cyan dot shows the value of L_1^{ICE} plotted along the real axis, and the green dot shows the ratio of $\{I_1^{\mathrm{ICE}}, I_2^{\mathrm{ICE}}\}$ to $\{P_1^{\mathrm{ICE}}, P_2^{\mathrm{ICE}}\}$, a test for how close the intermittent modes are to being a product of periodic and low-frequency modes. (A) shows an in phase regime, (B) shows and out of phase regime and (C) shows a transition regime. See movie 2 for a more illuminating time evolution.

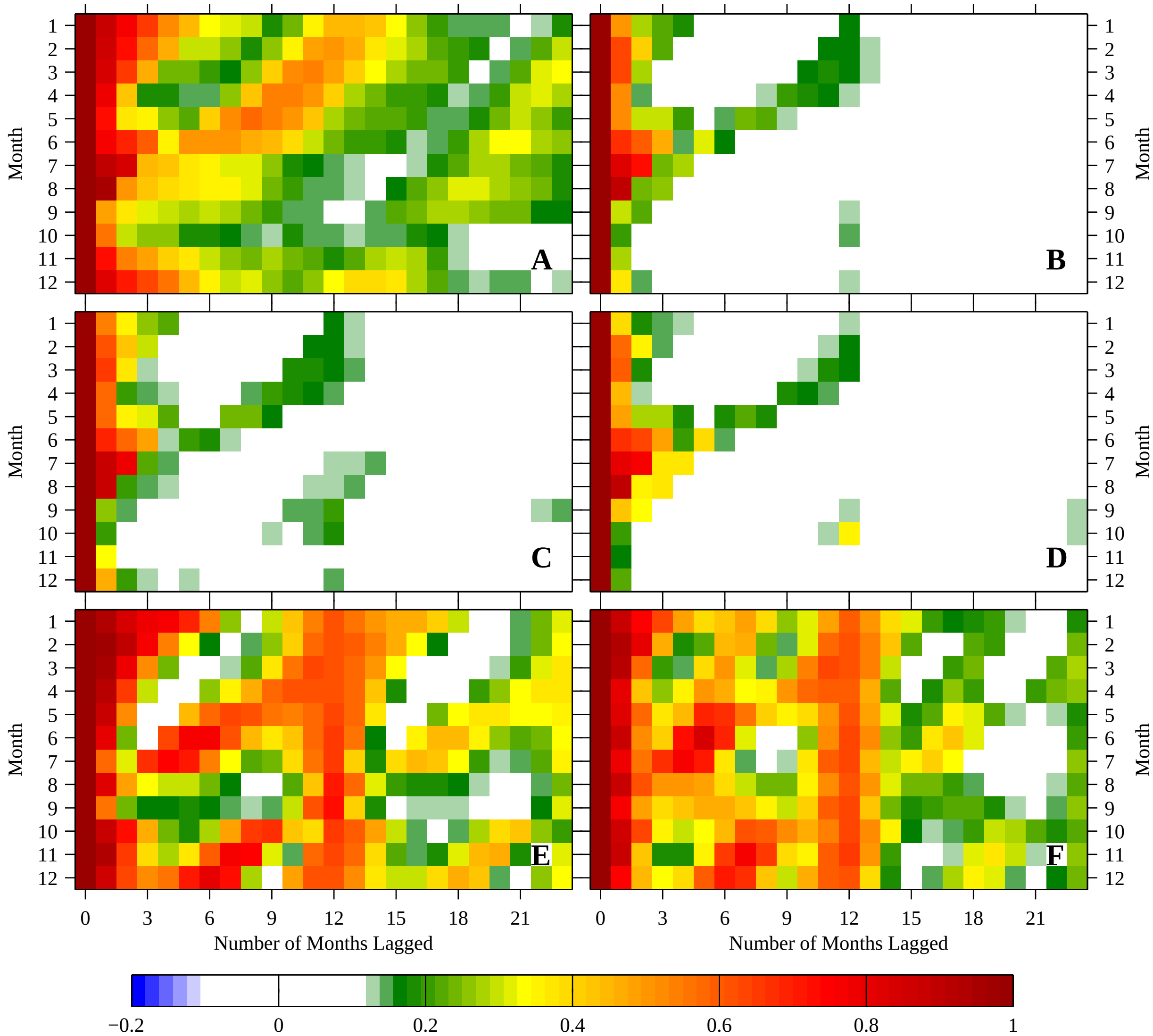

FIG. 8. Lagged correlations for North Pacific sea ice for all months and lags from 0 to 23 months. (A) shows the lagged correlation structure in total arctic sea ice area, computed following the methodology of BW. All other panels are lagged pattern correlations: (B) North Pacific with raw data; (C) and (D) are computed in the Bering and Okhotsk Seas, respectively, using raw data; (E) Bering Sea with modes $\{\mathbf{L}_1, \mathbf{I}_1, \mathbf{I}_2, \mathbf{I}_5, \mathbf{I}_6\}$; (F) Okhotsk Sea with modes $\{\mathbf{L}_2, \mathbf{I}_3, \mathbf{I}_4, \mathbf{I}_7, \mathbf{I}_8\}$. Colored boxes indicate correlations which are significant at the 95% level based on a t-test.

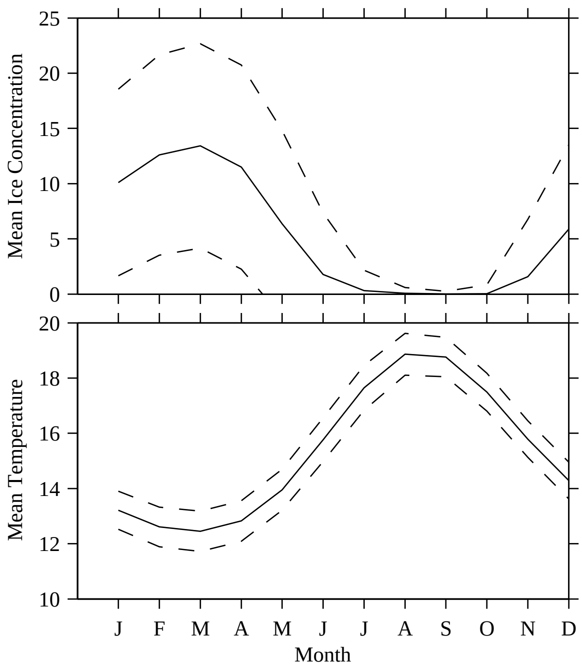

Fig. 9. Monthly mean sea ice concentration and SST from CCSM3, with the dashed line showing $\pm 1\sigma$. The SST variance is relatively uniform across all months, while the sea ice variance is much larger in high concentration months.

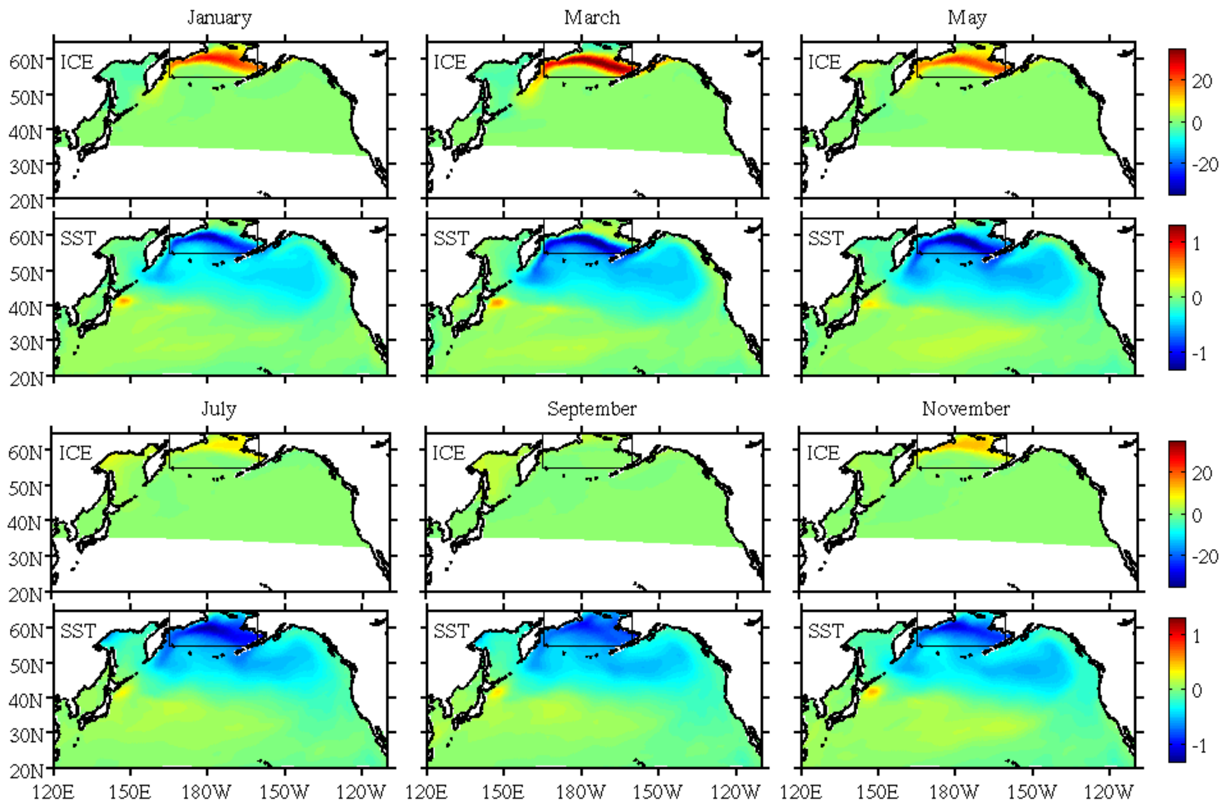

FIG. 10. Sea Ice and SST patterns for different months of the year, reconstructed using $\{\mathbf{L}_1, \mathbf{I}_1, \mathbf{I}_2, \mathbf{I}_5, \mathbf{I}_6\}$. These spatial patterns are composites, obtained by averaging over all years in which the NPGO is active, in its positive phase (defined as $L_2^{\mathrm{SST}} > 1.5$). The Bering Sea (boxed) exhibits a spring-fall sea ice reemergence. Positive spring sea ice anomalies imprint negative SST anomalies as they move northward during the melt season. The SST anomalies persist through the summer months, and when the ice returns in the growth season, the positive sea ice anomaly is reproduced. See movie 3 for the dynamic evolution of this mode family.

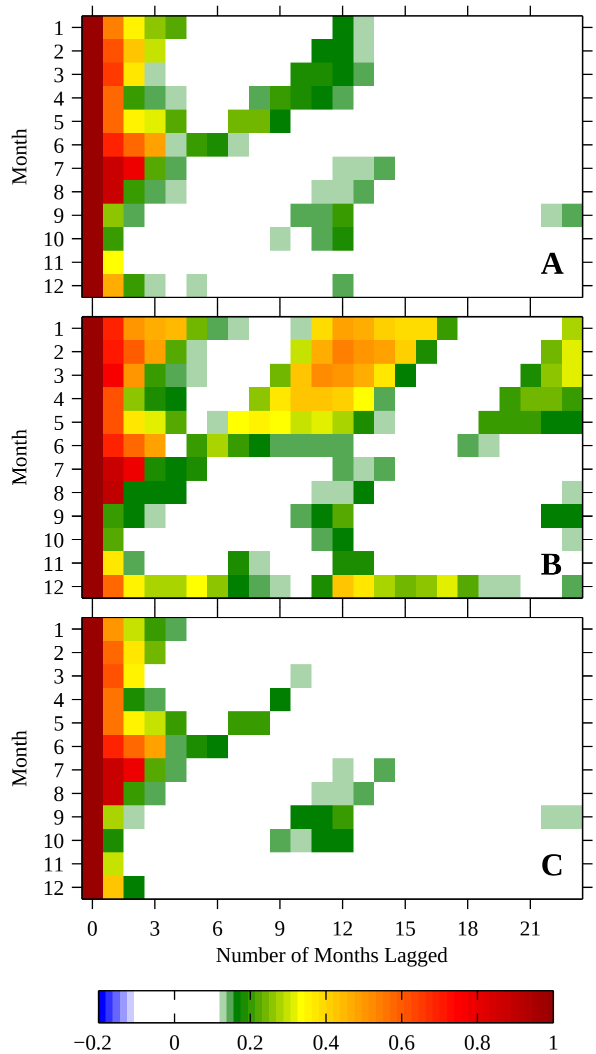

FIG. 11. Lagged pattern correlations for raw sea ice data in the Bering Sea, conditional on the NPGO principal component being active. (A) shows the Bering result with no conditioning. (B) and (C) show the Bering sea conditioned on $|L_2^{\mathrm{SST}}| > 1.5$ (all values above the 82nd percentile) and $|L_2^{\mathrm{SST}}| < 1$ (all values below the 65th percentile), respectively. Colored boxes indicate correlations which are significant at the 95% level based on a t-test.

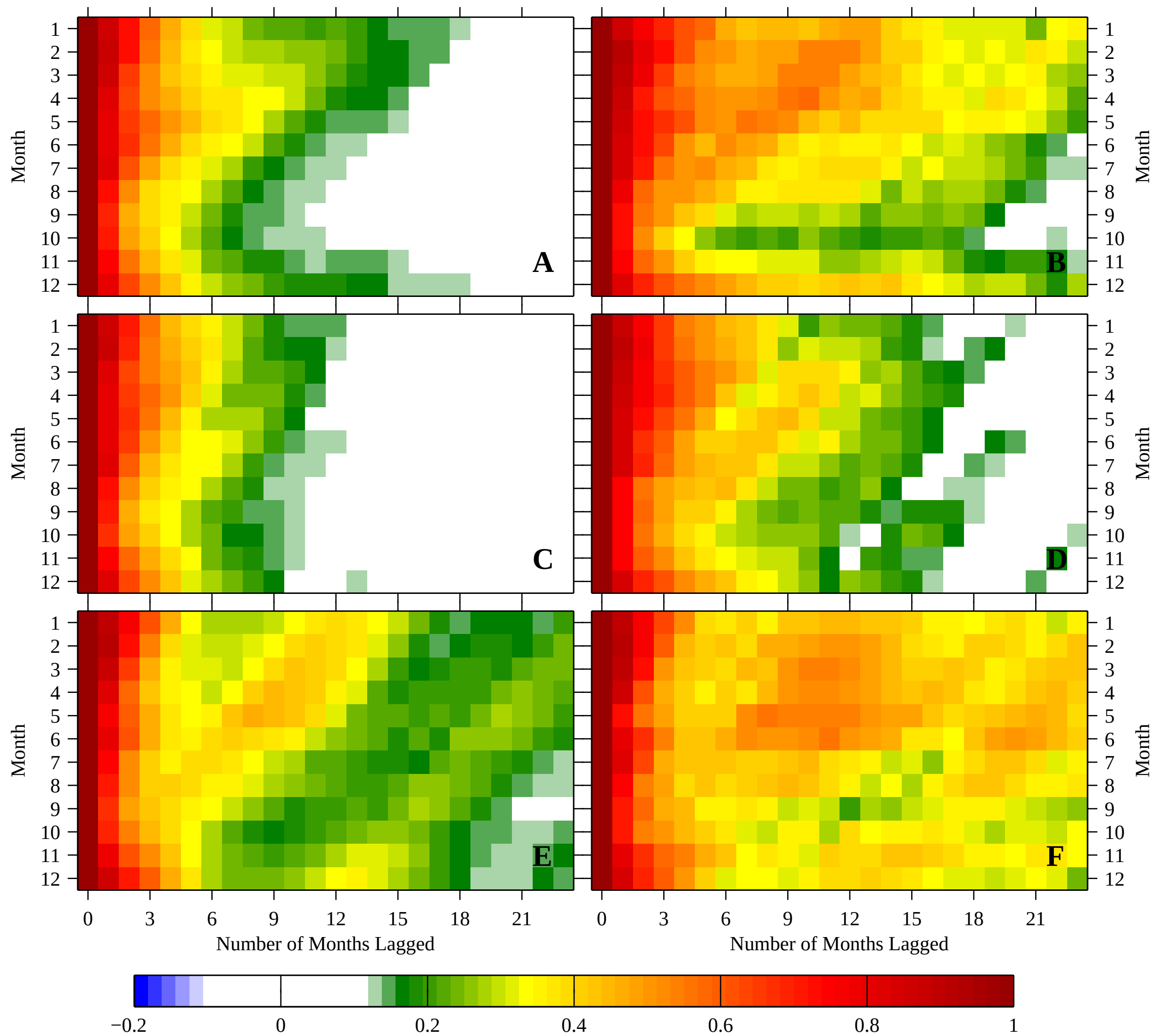

FIG. 12. Lagged correlations for North Pacific SST for all months and lags from 0 to 23 months. (A), (C), and (E) show lagged correlations of raw SST data in the central, eastern, and western Pacific, respectively. (B), (D), and (F), show lagged correlations in the same domains, conditional on $|L_1^{\mathrm{SST}}| > 1.5$ (all values above the 82nd percentile). Colored boxes indicate correlations which are significant at the 95% level based on a t-test.

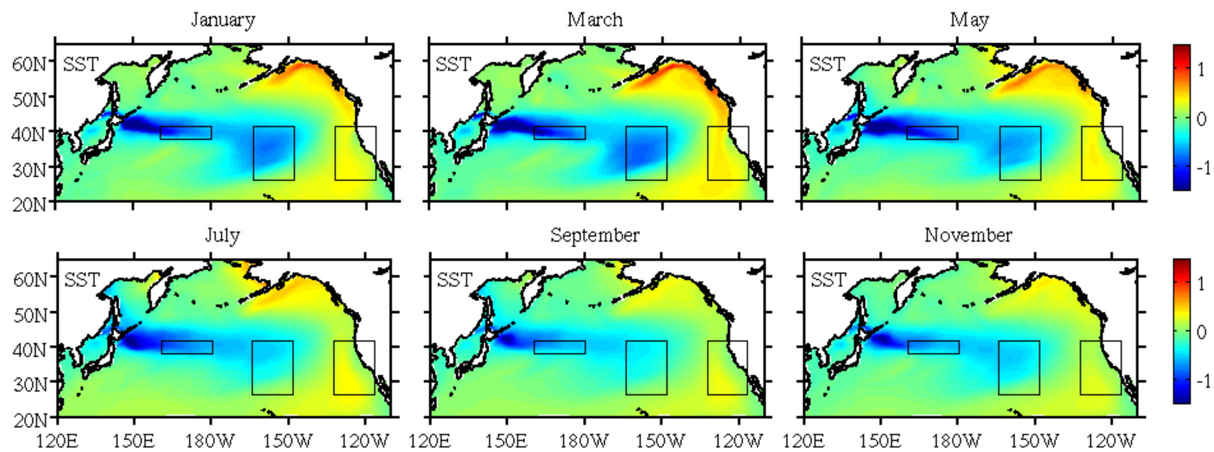

FIG. 13. SST patterns for different month of the year, reconstructed using $\{\mathbf{L}_2, \mathbf{I}_3, \mathbf{I}_4, \mathbf{I}_7, \mathbf{I}_8\}$. These spatial patterns are composites, obtained by averaging over all years in which the PDO is active, in its positive phase (defined as $L_1^{\mathrm{SST}} > 1.5$). The central, eastern, and western Pacific domains are boxed. The central pacific exhibits a reemergence of SST anomalies, while weaker reemergences are present in the eastern and western Pacific. The dynamic evolution of this mode family is shown in Movie 4.

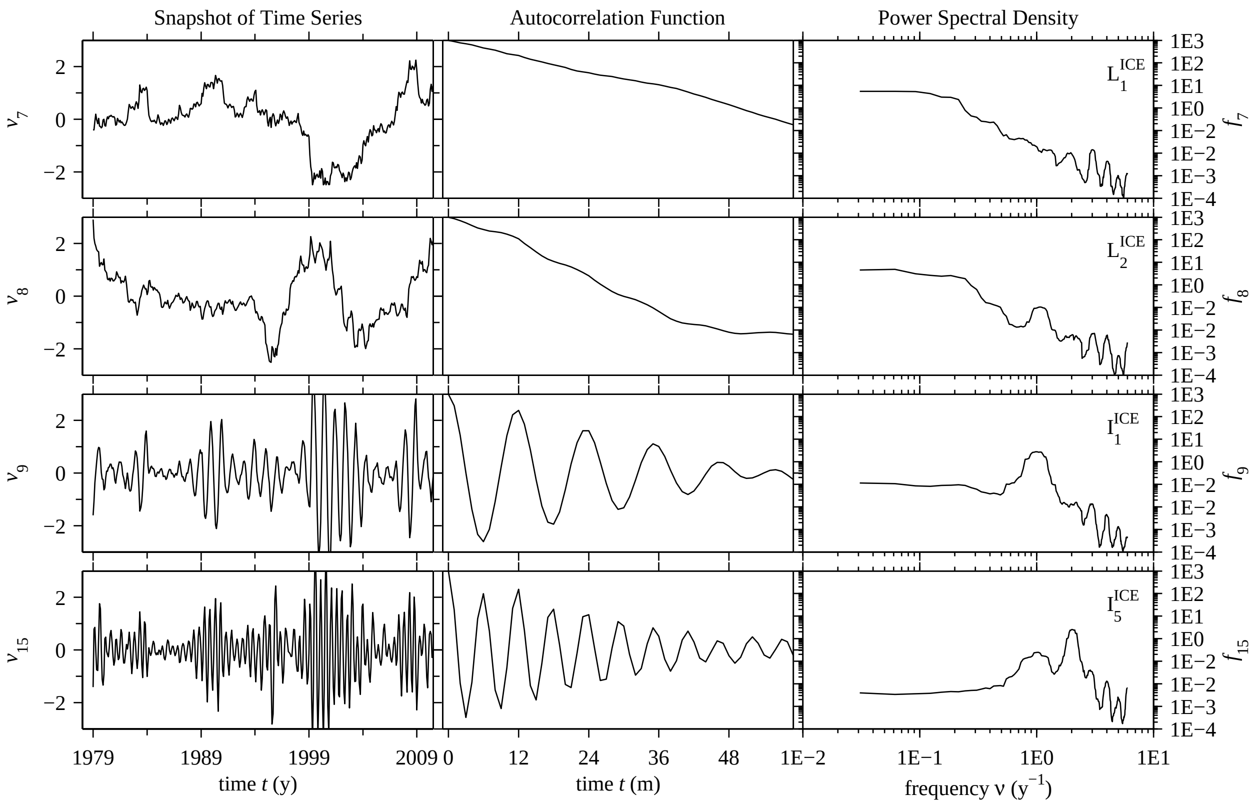

FIG. 14. Snapshots of the time series, power spectral density, and autocorrelation functions for the sea-ice PCs (v_k) from coupled NLSA on the HADISST dataset. Shown here are two low-frequency modes (L_1^{ICE} and L_2^{ICE}), an annual intermittent mode (I_1^{ICE}) and a semiannual intermittent mode (I_5^{ICE}). The autocorrelation vertical scale is [-1,1]. The power spectral densities (f_k) were estimated over the 34 year record via the multitaper method with time-bandwidth product $p = 6$ and $K = 2p - 1 = 11$ Slepian tapers.

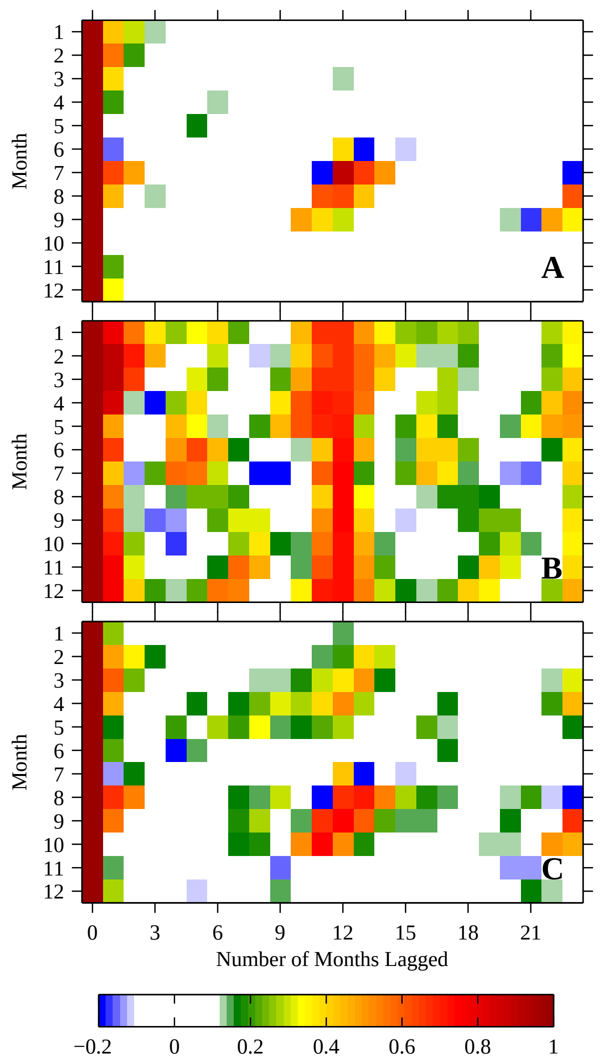

FIG. 15. Lagged correlations for North Pacific Sea Ice from the HADISST dataset for all months and lags from 0 to 23 months. (A) Shows lagged correlation for raw North Pacific sea ice data, (B) shows lagged correlations for the Bering Sea computed using the mode family $\{\mathbf{L}_1, \mathbf{I}_1, \mathbf{I}_2, \mathbf{I}_5, \mathbf{I}_6\}$, and (C) shows lagged correlations in the North Pacific for the raw data, conditional on $|L_2^{\mathrm{SST}}| > 1$ (all values above the 75th percentile). Colored boxes indicate correlations which are significant at the 95% level based on a t-test.

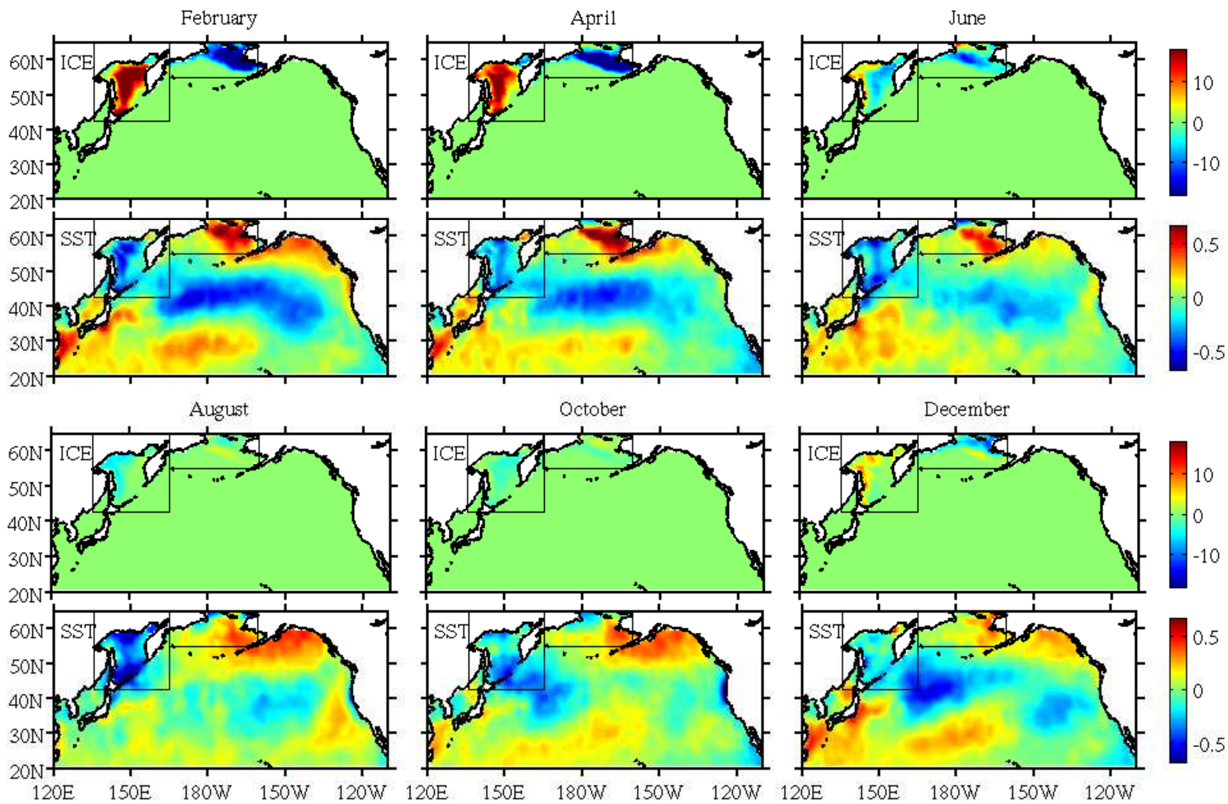

FIG. 16. Sea ice and SST patterns for year 2001, reconstructed from the HADISST dataset using modes $\{\mathbf{L}_1, \mathbf{I}_1, \mathbf{I}_2, \mathbf{I}_5, \mathbf{I}_6\}$. The Bering and Okhotsk Seas (both boxed) exhibit a spring-fall sea ice reemergence. See movie 5 for the dynamic evolution of this mode family.

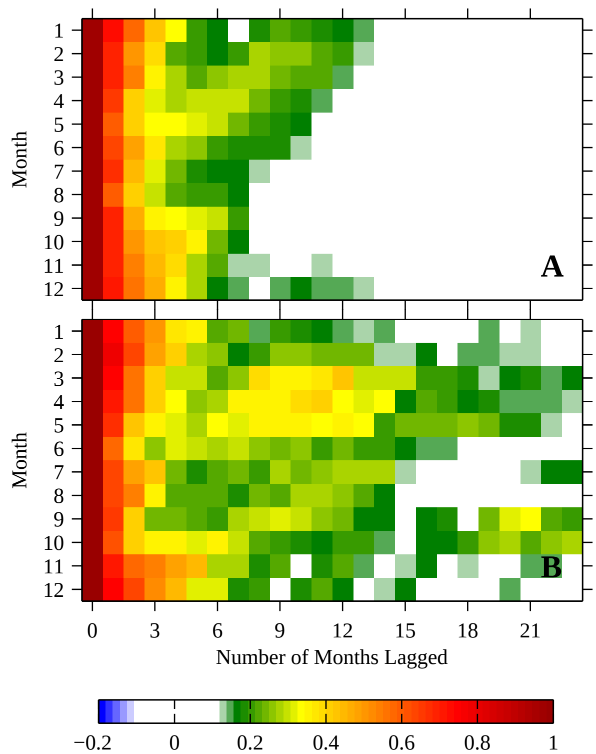

FIG. 17. Lagged correlations for North Pacific SST from the HADISST dataset for all months and lags from 0 to 23 months. (A) Shows lagged correlation for raw North Pacific SST data, (B) shows lagged correlations in the North Pacific for the raw data, conditional on $|L_1^{\mathrm{SST}}| > 1.5$ (all values above the 75th percentile). Colored boxes indicate correlations which are significant at the 95% level based on a t-test.

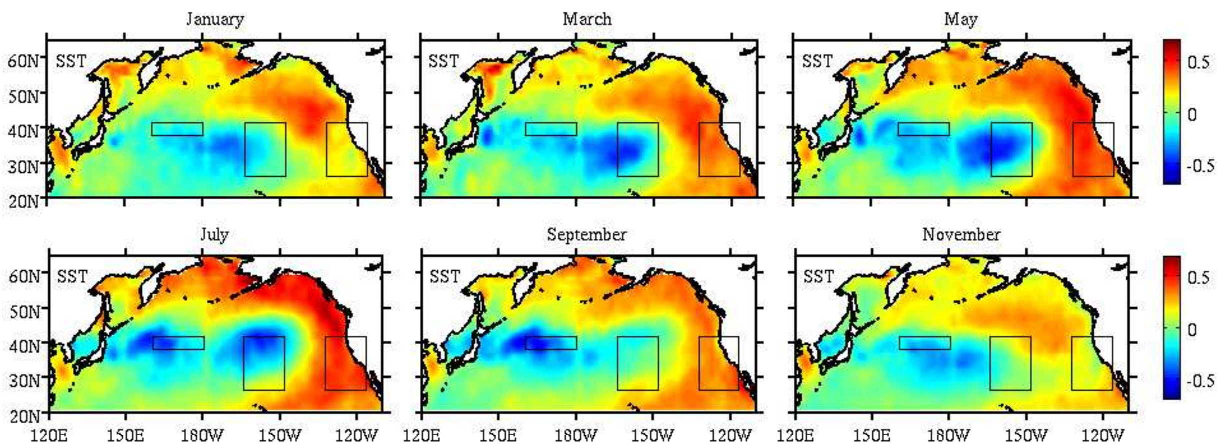

Fig. 18. SST patterns for year 2005, reconstructed from the HADISST dataset using modes $\{\mathbf{L}_2, \mathbf{I}_3, \mathbf{I}_4, \mathbf{I}_7, \mathbf{I}_8\}$. The central, eastern, and western Pacific domains are boxed. The central and eastern Pacific exhibit a reemergence of SST anomalies. See movie 6 for the dynamic evolution of this mode family.